2022-12

UAS ANALYSIS OF WAVE RUNUP AT COASTAL CALIFORNIA EPHEMERAL RIVERS

Plant, John T., III

Monterey, CA; Naval Postgraduate School

NAVAL POSTGRADUATE SCHOOL

MONTEREY, CALIFORNIA

THESIS

UAS ANALYSIS OF WAVE RUNUP AT COASTAL CALIFORNIA EPHEMERAL RIVERS

by

John T. Plant III

December 2022

Thesis Advisor: Mara S. Orescanin
Second Reader: Peter C. Chu

THIS PAGE INTENTIONALLY LEFT BLANK

REPORT DOCUMENTATION PAGE	*Form Approved OMB No. 0704-0188*

1. AGENCY USE ONLY *(Leave blank)*	**2. REPORT DATE** December 2022	**3. REPORT TYPE AND DATES COVERED** Master's thesis

4. TITLE AND SUBTITLE UAS ANALYSIS OF WAVE RUNUP AT COASTAL CALIFORNIA EPHEMERAL RIVERS	**5. FUNDING NUMBERS**
6. AUTHOR(S) John T. Plant III	
7. PERFORMING ORGANIZATION NAME(S) AND ADDRESS(ES) Naval Postgraduate School Monterey, CA 93943-5000	**8. PERFORMING ORGANIZATION REPORT NUMBER**
9. SPONSORING / MONITORING AGENCY NAME(S) AND ADDRESS(ES) N/A	**10. SPONSORING / MONITORING AGENCY REPORT NUMBER**

11. SUPPLEMENTARY NOTES The views expressed in this thesis are those of the author and do not reflect the official policy or position of the Department of Defense or the U.S. Government.

12a. DISTRIBUTION / AVAILABILITY STATEMENT Approved for public release. Distribution is unlimited.	**12b. DISTRIBUTION CODE** A

13. ABSTRACT (maximum 200 words)

Dynamical interactions between small-scale ephemeral river plumes and neighboring littoral regions directly affect sediment transport, nearshore morphology, bathymetry, and beach topography. Research into wave runup and river breaching events directly influences coastal engineering planning, and if current and accurate, can inform naval operational planning. Consistent and reliable data collection for these processes is challenging due to the active nature of both the surf and swash zones, and the rapid decay of data accuracy. This research expands previous wave runup and river breach studies, while simultaneously assessing the viability of using small commercially available unmanned aerial systems (UAS) as a nearshore research tool that is easily employable, low in cost, yet accurate. Existing empirical runup models have historically shown high predictive skill for gradually sloping smooth beaches; however, in many cases, do not account for rocky bottoms or surf-zone variations such as sand bars. Research sites were selected based on their distinct features related to alongshore profile, bathymetry, and bottom type. The main result was that models do not predict runup accurately in complex coastal regions that include rocky bottoms, river mouths, or sandbars. The UAS imagery analysis reinforced limitations of utilizing these models and demonstrated a means to identify unique surf-zone features, and accurately capture runup excursions at diverse beaches.

14. SUBJECT TERMS wave runup, nearshore morphology, ephemeral river, unmanned systems	**15. NUMBER OF PAGES** 77
	16. PRICE CODE

17. SECURITY CLASSIFICATION OF REPORT	**18. SECURITY CLASSIFICATION OF THIS PAGE**	**19. SECURITY CLASSIFICATION OF ABSTRACT**	**20. LIMITATION OF ABSTRACT**
Unclassified	Unclassified	Unclassified	UU

NSN 7540-01-280-5500

Standard Form 298 (Rev. 2-89)
Prescribed by ANSI Std. 239-18

THIS PAGE INTENTIONALLY LEFT BLANK

Approved for public release. Distribution is unlimited.

UAS ANALYSIS OF WAVE RUNUP AT COASTAL CALIFORNIA EPHEMERAL RIVERS

John T. Plant III
Lieutenant, United States Navy
BS, Old Dominion University, 2014

Submitted in partial fulfillment of the
requirements for the degree of

MASTER OF SCIENCE IN METEOROLOGY AND PHYSICAL OCEANOGRAPHY

from the

NAVAL POSTGRADUATE SCHOOL
December 2022

Approved by: Mara S. Orescanin
Advisor

Peter C. Chu
Second Reader

Peter C. Chu
Chair, Department of Oceanography

THIS PAGE INTENTIONALLY LEFT BLANK

ABSTRACT

Dynamical interactions between small-scale ephemeral river plumes and neighboring littoral regions directly affect sediment transport, nearshore morphology, bathymetry, and beach topography. Research into wave runup and river breaching events directly influences coastal engineering planning, and if current and accurate, can inform naval operational planning. Consistent and reliable data collection for these processes is challenging due to the active nature of both the surf and swash zones, and the rapid decay of data accuracy. This research expands previous wave runup and river breach studies, while simultaneously assessing the viability of using small commercially available unmanned aerial systems (UAS) as a nearshore research tool that is easily employable, low in cost, yet accurate. Existing empirical runup models have historically shown high predictive skill for gradually sloping smooth beaches; however, in many cases, do not account for rocky bottoms or surf-zone variations such as sand bars. Research sites were selected based on their distinct features related to alongshore profile, bathymetry, and bottom type. The main result was that models do not predict runup accurately in complex coastal regions that include rocky bottoms, river mouths, or sandbars. The UAS imagery analysis reinforced limitations of utilizing these models and demonstrated a means to identify unique surf-zone features, and accurately capture runup excursions at diverse beaches.

THIS PAGE INTENTIONALLY LEFT BLANK

TABLE OF CONTENTS

I. MOTIVATION 1

II. INTRODUCTION 3

A. BACKGROUND 3
B. WAVE RUNUP 4
C. EPHEMERAL RIVERS 6
D. UAS FOR NEARSHORE ANALYSIS 8

III. METHODOLOGY 11

A. FIELD RESEARCH SITES 11
B. FIELD DATA COLLECTION 12
C. UAS WAVE RUNUP OBSERVATION 13
D. TOPOGRAPHIC AND BATHYMETRIC SURVEYS 14
E. DATA PROCESSING 16
F. EMPIRICAL METHODS 19

IV. ANALYSIS AND RESULTS 23

A. TOPOGRAPHY AND BATHYMETRY 23
B. RUNUP OBSERVATIONS 27
C. RESULTS SUMMARY 38

V. DISCUSSION 41

A. EMPIRICAL MODEL OBSERVATIONS 41
B. SOURCES OF ERROR AND POTENTIAL REMEDIES 41
C. DECREASING THE HUMAN FOOTPRINT 45

VI. CONCLUSION 47

APPENDIX A. CARMEL RUNUP DATA 49

APPENDIX B. PAJARO RUNUP DATA 51

LIST OF REFERENCES 53

INITIAL DISTRIBUTION LIST 59

THIS PAGE INTENTIONALLY LEFT BLANK

LIST OF FIGURES

Figure 1. Study area surf zone widths and shape of the study areas. Carmel River site (a) and Pajaro River site (b)..... 6

Figure 2. Satellite imagery of Pajaro River breach September 2017 (a) and November 2019 (b). Adapted from Google Earth (2022)..... 7

Figure 3. Global distribution of ICOLLS. Source: McSweeney et al. (2017). 8

Figure 4. Carmel and Pajaro rivers' positions relative to Monterey Bay. Adapted from Google Earth (2022). 12

Figure 5. DJI Inspire 1 quadcopter..... 13

Figure 6. GNSS receiver mapping a GCP (a) and GCP spread (yellow circles) for UAS collection flight (b)..... 14

Figure 7. GPS walking survey set up and antenna height measurement..... 15

Figure 8. CIRN imagery output showing transect placement (a), wave propagation time series for a single transect (b), and edge detection output showing runup position relative to swash zone (c)..... 17

Figure 9. Agisoft mapping survey imagery output..... 18

Figure 10. SMS DEMS output from Agisoft with walking survey (dark green line) and runup observation transects (purple and bright green) overlayed for Carmel River (a) and Pajaro River (b). 19

Figure 11. Rocky portion of Carmel River to the south of breach. 24

Figure 12. Foreshore transect slopes for Carmel River (03Dec21) (a), and Pajaro River (15Apr22) (b)..... 26

Figure 13. Bathymetry and topographic measurement surveys for the Carmel and Pajaro river sites, (a) and (b), respectively. Depth vs. distance bathymetry plot for both sites is shown in (c)..... 27

Figure 14. Carmel River observations for 03 December 2021..... 29

Figure 15. Carmel River observations for 15 January 2022..... 29

Figure 16. Carmel River observations for 10 March 2022..... 30

Figure 17. Carmel River observations for 15 June 2022..... 30

Figure 18. Carmel River observations for 13 July 2022 30
Figure 19. Pajaro River observations for 18 February 2022 31
Figure 20. Pajaro River observations for 11 March 2022 31
Figure 21. Pajaro River observations for 15 April 2022 31
Figure 22. Carmel River $R_{O2\%}$ observed values (a) and $R_{O2\%}$ regression to $R_{M2\%}$ (b) 33
Figure 23. Pajaro River $R_{O2\%}$ values (a) and $R_{O2\%}$ regression to $R_{M2\%}$ (b) 34
Figure 24. $R_{O2\%}$ and $R_{M2\%}$ regression to ξ for Carmel (a) and Pajaro (b) rivers 35
Figure 25. Outgoing Carmel River plume on 14 January 2022 (a) and 10 March 2022 (b) 43
Figure 26. Outgoing Pajaro River plume on 11 March 2022 (a) and 15 April 2022 (b) 43

LIST OF TABLES

Table 1. Wave height, tidal, and meteorological data sources 13

Table 2. Carmel River southern and northern transect comparison 25

Table 3. Pajaro River southern and northern transect comparison 25

Table 4. Collection dates, durations, tidal stage, and measured water levels 28

Table 5. Carmel River r and σ_{xy} values for observations and model output by transect location relative to breach 33

Table 6. Pajaro River r and σ_{xy} values for observations and model output by transect location relative to breach 34

Table 7. R^2 values for Carmel River $R_{2\%}$ to ξ regression 36

Table 8. R^2 values for Pajaro River $R_{2\%}$ to ξ regression 36

Table 9. R^2 values for Carmel River $R_{2\%}$ to H_S regression 37

Table 10. R^2 values for Pajaro River $R_{2\%}$ to H_S regression 37

Table 11. R^2 values for Carmel River $R_{2\%}$ to β regression 37

Table 12. R^2 values for Pajaro River $R_{2\%}$ to β regression 38

THIS PAGE INTENTIONALLY LEFT BLANK

LIST OF ACRONYMS AND ABBREVIATIONS

CIRN	Coastal Imaging Research Network
CNMOC	Commander Naval Meteorology and Oceanography Command
COTS	Commercial-Off-The-Shelf
DEM	Digital Elevation Model
DJI	Da-Jiang Innovations
DMO	distributed maritime operations
DOD	Department of Defense
DON	Department of the Navy
DPD	dominant wave period
DTM	digital terrain model
FoV	field of view
GCP	ground control point
GNSS	Global Navigation Satellite System
GPS	global positioning system
H_S	significant wave height
LiDAR	Light Detection and Ranging
METAR	Meteorological Terminal Air Report
MWD	mean wave direction
NAVD88	North American Vertical Datum of 1988
NDBC	National Data Buoy Center
NOAA	National Oceanographic and Atmospheric Administration
$R_{2\%}$	2% Runup Extent
RMSE	root mean square error
UAS	unmanned aerial systems
UUS	unmanned underwater systems
UxS	unmanned systems
SMS	Surface-water Measuring Software
TAF	Terminal Area Forecast

THIS PAGE INTENTIONALLY LEFT BLANK

ACKNOWLEDGMENTS

My sincerest thanks to Dr. Mara Orescanin for all her guidance, mentorship, and encouragement while conducting this research, during a challenging period of COVID-19 protocols and restrictions. Her passion and depth of knowledge for her field truly made this an enjoyable experience, both in the field and in the classroom. I greatly value both our professional relationship and the friendship that has developed. Thank you as well to Dr. Peter Chu, my second reader for not only reviewing and critiquing my paper but the knowledge and experience he shared in the classroom.

Additionally, I would like to thank the following:

Mike Cook and Paul Jessen, for the countless hours of field support, and MATLAB coding assistance.

Dr. Angelica Rodriguez and the leadership at NIWC-PAC, for providing a fellowship, which enabled me to travel to San Diego and meet with and learn from a wide range of nearshore researchers

The Coastal Research Group at Scripps Institute of Oceanography, for taking the time to meet in person as well as virtually, to share their knowledge and experience and helping me develop and mature my research effort

Dr. Britany Bruder, Army Corps of Engineers, for lending her experience and source code toolbox for UAS nearshore image processing.

I would also like to thank my cohort of fellow naval METOC officers, for providing support and friendship during our time here at Naval Postgraduate School. We overcame a challenging environment and succeeded together!

Most importantly I would like to say thank you to my family, especially my wife, Lori, who provided love and support throughout this journey. I wouldn't have finished without you.

THIS PAGE INTENTIONALLY LEFT BLANK

I. MOTIVATION

In March of 2021, the Department of the Navy released the Unmanned Campaign Framework (Department of the Navy 2021). While the primary focus of this document is to drive integration and expansion of Unmanned Systems (UxS) in support of Distributed Maritime Operations (DMO), utilization of this capability also provides a more agile method to gather timely and operationally relevant scientific information to "shape data into decisions," according to Commander Naval Meteorology and Oceanography Command (CNMOC), (2018), which directly supports the larger Navy objectives. Prior to the release of the Navy's Unmanned Campaign Framework, CNMOC laid out priorities for the community with a 2018 strategic plan. Within the target objectives for the strategic plan's second priority, Capability, are three specific focus areas which are addressed within the scope of this study. These include advancing UxS to "increase global ocean and atmospheric deployments," "rapidly assimilating on-scene environmental data from Navy, Joint and other trusted source sensors to exploit operational and tactical advantages in real-time across widely distributed maritime forces," and increasing "forecast accuracy in areas where Naval Power matters" per Commander Naval Meteorology and Oceanography Command (2018).

The Navy currently uses an extensive array of Unmanned Underwater Systems (UUS) of various sizes and capabilities. CNMOC is a leading practitioner of these platforms, utilizing them for oceanographic research around the globe. These UUS conduct a wide expanse of oceanographic research functions yet can be extremely expensive and require extensive training. The Department of the Navy (DON) currently does not have an enlisted rating dedicated to the operation of these systems. Due to this fact, military personnel who operate them often rotate out of associated assignments and move on with their careers into positions where UUS skills are not required.

Unmanned Aerial Systems (UAS) are not used as prevalently within the community. Until recently there were significant limitations on key features such as endurance and payload capacity/capability. The cost of UAS has significantly decreased over the last decade with many extremely capable systems now available for as low as a

couple thousand dollars. More importantly, these systems are getting easier to fly, with training taking as little as a day to learn basic flight controls and mission planning software. Additionally, for the smaller quadcopters, the basic control and understanding of flight dynamics are extremely similar across a large swath of platforms, allowing for easy retraining and integration of new platforms. UAS are no longer simply an emerging capability, they are an established technology that is rapidly being integrated across countless fields. Identifying current oceanographic research requirements, such as nearshore analysis, which can be augmented with UAS will provide the Navy with fiscal and manpower efficiencies, and directly enhance current and future operational planning efforts.

The Navy has a vested interest in monitoring and predicting environmental dynamics within the littoral regions, from both operational and engineering perspective. Operationally, conducting amphibious operations is a fundamental mission for the Navy no matter it be for Marines or maritime special operations forces. Understanding that the coastal region is being continuously modified, and knowing how best to predict its active state, will provide operational planners the ability to place forces ashore, safely and efficiently anywhere on the globe. Engineering considerations for naval base construction and protection also require a consistent and up-to-date awareness of how the ocean is changing our coastlines. As wave action and river breaches move sediment along the shoreline, it affects the magnitude of wave energy moving alongshore. Coupled with increasing sea levels, this alteration of beach morphology must be factored into short- and long-term planning considerations for coastal infrastructure.

II. INTRODUCTION

A. BACKGROUND

The nearshore environment is a dynamic region, susceptible to rapid hydrodynamic and morphological change based off a myriad of physical environmental factors. Understanding, quantifying, and modeling the interacting forces that drive these changes is essential for environmental hazard, coastal engineering, and operational planning. Wave energy and the associated runup are key factors that significantly alter both beach topography and the underlying bathymetry. Efforts to better understand the motion of waves as they approach the shore, and to improve the accuracy of numerical predictions associated with it, have been a research focus going back over 70 years, such as in studies by Iribarren and Nogales (1949) and Battjes (1974). Despite the extensive amount of research, there remain many difficulties in accurately predicting wave runup along certain types of coastlines, including rocky areas or around river mouths.

Nearshore regions, and more specifically, the coastal areas where rivers breach into the sea, can undergo significant and sudden morphological changes. These influences can be most pronounced on the region of the beach just above the shoreline, and on the underwater bathymetry within the surf and shoaling zones. A substantial amount of research has been dedicated to understanding these morphodynamics and how the waves and currents affect the underlying bathymetry and sediment transport.

Owing to the volatile nature of the surf zone, the ability to actively monitor and predict nearshore processes, specifically wave runup, is a constant challenge. Multiple factors, including scale, wave action, meteorological effects, small temporal periods within which the observation areas change, and technological limitations contribute to this challenge. The predominant consideration is overcoming the impact of winds and wave motion, whose intensity can change rapidly, resulting in fast-developing alterations within this region. Technology advances at an ever-quickening pace, providing new tools that can be leveraged for increased and improved data collection. According to the National Air and Space Administration's (NASA) Science webpage, the Earth has

approximately 372,000 miles of coastline. The sheer span of this area necessitates having a multitude of methods to conduct observations and data collection of priority regions. Past methods of environmental sensing are not always the most effective to gather oceanographic data. Ibateca et al. (2018) provide a historical progression of the various measurement methods including resistance wires, pressure sensors, and ultrasonic distance meters, which all required the physical presence of instruments within the surf zone. In the past few decades, methods such as the ARGUS program out of Oregon State University's Coastal Imaging Lab have been increasingly used. These techniques include fixed station video imaging as shown by Holman and Stanly (2007), as well as Light Detection and Ranging (LiDAR) observations as conducted by Palmsten and Brodie (2022) and Brodie et al. (2015). In 2019, Bruder et al. demonstrated the expeditionary capability of a miniaturized ARGUS system which could be rapidly deployed, overcoming the limitations of the larger fixed stations. My study continues that line of effort and demonstrates the ability to leverage commercial-off-the-shelf (COTS) UAS with their organic onboard cameras to provide rapid and accurate measurements of wave runup at multiple locations along the California coast.

B. WAVE RUNUP

Wave runup is defined across numerous studies as the highest vertical extent that ocean water reaches as it advances up the shoreline (Hunt 1959; Battjes 1971; Stockdon et al. 2006; Laudier et al. 2011; Orescanin and Scooler 2018). As wave energy approaches the shoreline, it is dissipated via several means including reflection, surf zone turbulence following wave breaking, and conversion to potential energy in the form of wave setup and runup (Battjes 1971). How this wave energy acts, is largely dependent on a combination of the beach slope and incoming wave characteristics. This relationship was first discussed in 1949 and formally parameterized as the Iribarren Number (ξ), or "surf similarity parameter" in 1954 (Equation 1) (Iribarren and Nogales 1949; Battjes 1974). To the present day, it serves as a foundation for a substantial quantity of nearshore wave studies. Quantifying and predicting runup values are critical to understanding the morphodynamical changes that are occurring, and how this will change with sea level

variability. These changes drive beach erosion, bathymetric changes from large-scale sediment transport, and saltwater intrusion into coastal lagoons and estuaries.

The research dedicated toward quantifying wave runup has progressed significantly since Hunt proposed his first empirical model for calculating wave runup in 1959. Since then, research efforts have provided steady improvements on the mathematical derivations and expanded to account for unique variables such as beach type (reflective or dissipative) (Stockdon et al. 2006), differences in bathymetry between the nearshore and foreshore (da Silva et al. 2020), and tidal influences (Vousdoukas et al. 2012). Through much of the literature, the key environmental parameters to determine runup remain what Battjes initially parameterized in 1974, factors of wave height (H), wavelength (L), beach slope (β).

$$\xi = \frac{\beta}{(\frac{H}{L})^{\frac{1}{2}}} \tag{1}$$

The slope of the beach has been shown to have a particular significance on the way waves break, affecting how the wave energy is dissipated (Wiegel 1964; Galvin 1968) and determining the ultimate level of wave runup. As reflective beaches tend to result in waves breaking closer to shore, kinetic energy is conserved longer and closer to the beach relative to dissipative beaches. This correlates well with observations that show larger slope beaches tend to result in higher observed runup values, as the larger remaining kinetic energy pushes the wave higher up onto the shore. A standard parameterization to delineate between the reflective and dissipative beaches, is an Iribarren of $\xi<0.3$ for dissipative beaches and $\xi>0.3$ for reflective beaches (Stockdon et al. 2006). For dissipative beaches, wave height has been found to have the highest effect on runup values, as opposed to the beach slope for reflective beaches (Nielsen and Hanslow 1991; Ruessink et al. 1998; Ruggiero et al. 2001). Most existing models factor beach slope prominently; but, based on the decreased effect of slope on runup at dissipative beaches, some existing models have suggested variations based solely on the wave characteristics (Carlson, 1987; Stockdon et al. 2006). A smaller, and more recent, subset of wave runup studies have considered the interaction of incoming wave energy as

it passes over differing bottom types, specifically rocky bottoms, and how they affect the incoming wave energy (Dodet et al. 2018; Holländer 2022).

The Carmel and Pajaro rivers were selected for this study due to the large differences in their respective bathymetric and foreshore profiles. The beach at Pajaro River has the appearance of a dissipative profile, with a wide and straight beach with a gentle slope that continues into the surf zone. The beach at Carmel River has the characteristics of a reflective profile, with a relatively steeper foreshore and nearshore bathymetry, coupled with a concave beach profile and a narrow surf zone (Figure 1).

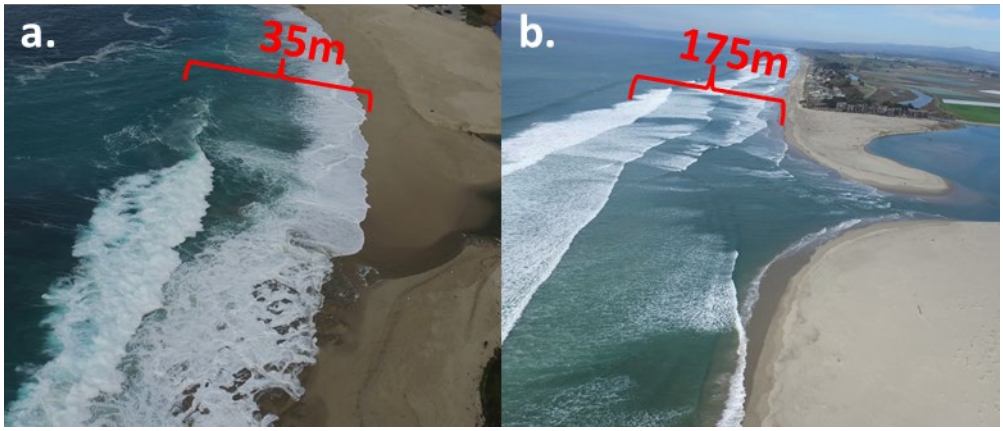

Figure 1. Study area surf zone widths and shape of the study areas. Carmel River site (a) and Pajaro River site (b).

C. EPHEMERAL RIVERS

Ephemeral rivers, also called bar-built estuaries and intermittently closed/open lakes and lagoons, are defined as rivers that cease to flow during portions of the year, and in some cases can periodically dry completely. These rivers are found near the coast, typically in "Mediterranean" climates, and as their primary source of water is from runoff following precipitation events, their ability to break through, or breach, to the sea is driven by the wet-dry cycle as mentioned by Orescanin and Scooler (2018) and Blackman et al. (2021). The counteracting influence of forces, specifically wave energy and river flow, drive sediment buildup alongshore above and below the shoreline, and can drastically change the shape, slope, and composition of these regions. Figure 2 shows

the migration of the river mouth of the Pajaro River over a two-year span. Breaches in these areas are caused by both artificial and natural methods. When an associated lagoon builds up a high enough water level, it can penetrate through the beach, or when a small channel is formed by river water seepage a small channel can form. These breaches can occur suddenly and rapidly form large high-velocity river mouths. The beaches can be dug out to create an artificial channel, enabling engineers to better manage the lagoon's water level as a flood prevention measure, as well as to control when the breaches occur (Kraus et al. 2002; Behrens et al. 2013; Orescanin et al. 2021).

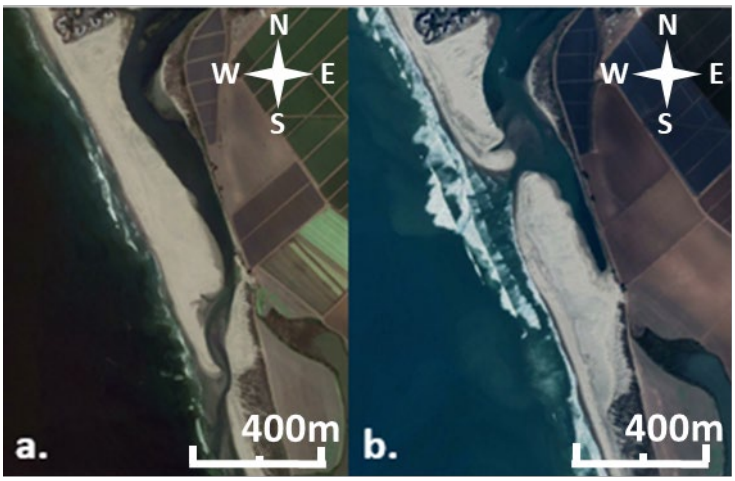

Figure 2. Satellite imagery of Pajaro River breach September 2017 (a) and November 2019 (b). Adapted from Google Earth (2022).

McSweeney et al. (2017) concluded that there are 1,400 of these types of intermittently closed/open regions located around the world which are highlighted in Figure 3. Large numbers of these systems are present along the west coast of the United States, including south along the Mexican coastline. Around the Monterey Bay region, stretching from Carmel River State Beach to Natural Bridges State Beach near Santa Cruz, there are seven intermittently breached rivers, including the two in this study, Carmel River and Pajaro River.

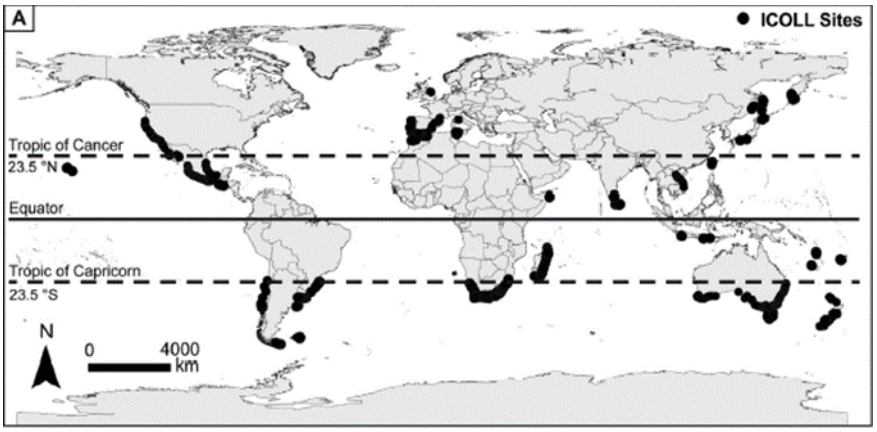

Figure 3. Global distribution of ICOLLS. Source: McSweeney et al. (2017).

Many of these river mouths are not influenced by permanent human engineering influences, thus the extent of the river sediment discharge during breach periods is directly affected by the interaction of the incoming wave energy and the outgoing river flow. Closures occur as tidal energy and large waves propagate in and drop sediment at the river mouth. Generally, wave energy is the predominant influence on morphological changes within the nearshore, specifically in the surf zone region. The associated circulation from this interaction of the waves and the shoreline is the primary influence on the direction and penetration level of the outgoing river plume. (Kastner et al. 2019). Propagation direction as well as the penetration depth of the river plume sediment can alter where sand bars develop both near the river mouth and in the alongshore direction (Aubrey and Speer 1984; Orescanin et al. 2021). There is a large body of research related to wave runup empirical calculations; however, due to the large morphological differences observable at beaches around the world, the existing models can result in significant errors without site-specific parametrization for multiple variables.

D. UAS FOR NEARSHORE ANALYSIS

Over the last decade, considerable research has been conducted demonstrating methods to utilize UAS for nearshore analysis. A significant quantity of this research has been focused on coastal bathymetry (Holeman et al. 2011; Janušaitė et al. 2019; Brodie et al. 2019; Lange et al. 2022). A smaller subset has focused on studying nearshore wave

dynamics, specifically runup (Brodie et al. 2015; Holman et al. 2017; Brodie et al. 2019). A key limitation of small UAS has been endurance, which is directly impacted by the weight of the system and any attached payloads. UAS were previously too small to carry the necessary GPS and internal measurement hardware that were necessary for accurate measurements (Holland et al. 2010). Technology has now advanced to the point where the average person can purchase highly capable platforms with extremely accurate station keeping and high-resolution onboard cameras at a very low price point. These systems offer the capability for researchers to conduct nearshore analysis in areas where fixed stations are not present, or are cost-prohibitive to install, and areas that would previously have been difficult to physically access on foot. Additionally, the utilization of UAS can offer the ability to conduct research in areas that have increased levels of environmental protections in place preventing significant human presence.

THIS PAGE INTENTIONALLY LEFT BLANK

III. METHODOLOGY

A. FIELD RESEARCH SITES

Two central coastal California ephemeral rivers were selected for observations and data collection, Pajaro River and Carmel River, as shown in Figure 4. The Pajaro River feeds into Monterey Bay along the border between Santa Cruz and Monterey Counties. It is the largest watershed between San Francisco and the Salinas River watershed, encompassing approximately 3,400 km^2 spread across four California counties, with the longest reach being about 11.42 km up to its outlet at Chittenden Pass (Pajaro River Watershed Integrated Regional Water Management 2014). It remains open to Monterey Bay for much of the year, typically closing during the drier periods of the summer to fall and then breaching and remaining open following the initial precipitation event which typically occurs in the early winter timeframe.

The Carmel River, located just south of Monterey Bay in Carmel Bay, is approximately 58 km long (Orescanin and Schooler 2018) and flows into a lagoon that sits approximately 100 meters inland from Carmel Bay. Carmel River historically remains closed unless preceded by a significant precipitation event, causing river discharge levels to rise, resulting in water levels growing in the lagoon. Substantial related research has been conducted at this location (Laudier et al. 2011; Orescanin and Scooler 2018; Orescanin et al. 2021), providing a foundation for this research effort.

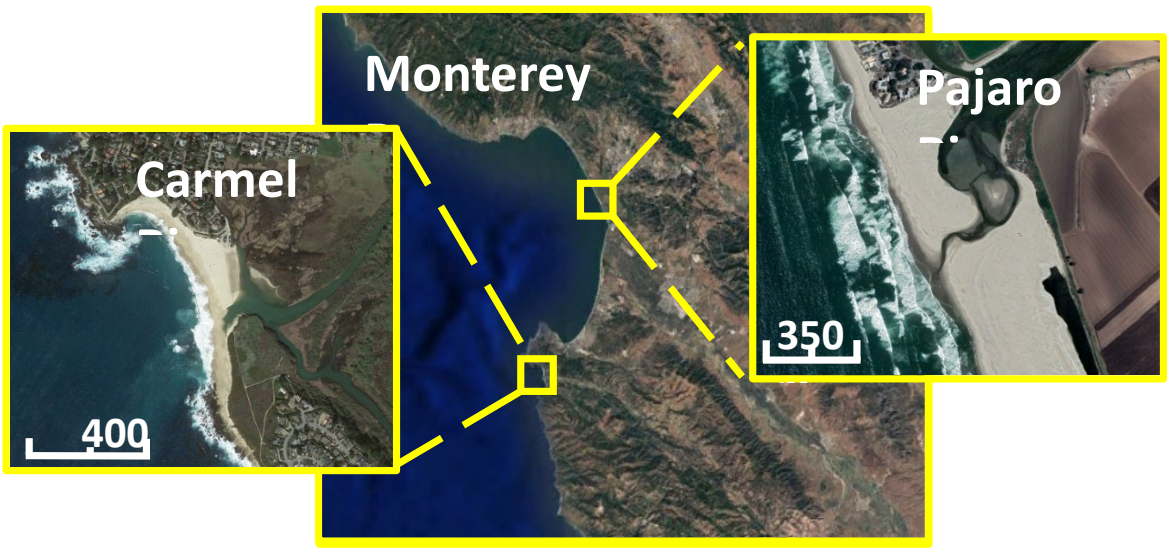

Figure 4. Carmel and Pajaro rivers' positions relative to Monterey Bay. Adapted from Google Earth (2022).

B. FIELD DATA COLLECTION

Field research consisted of three specific data collections: UAS wave runup observation, topographic survey, and nearshore bathymetry survey. Wave runup and topographic methods were conducted concurrently, while bathymetric surveys were conducted separately based on sea state conditions. Oceanographic data, specifically Significant Wave Height (Hs), Dominant Wave Period (DWP), and Mean Wave Direction (WMD), were compiled from the nearest offshore buoy utilizing the National Data Buoy Center (NDBC) page. National Oceanographic and Atmospheric Administration's (NOAA) Tides and Currents database was used to determine tidal periods, as collection timeframes were determined, and data was referenced against NAVD88 and factored into wave runup calculations. Timeframes for collection were selected to gather data across multiple tidal phases at each site. Wind data (velocity and direction) was compiled from the National Weather Center's Aviation Weather Center portal using the nearest Meteorological Terminal Air Report (METAR) and Terminal Area Forecast (TAF) data. Wind data was used to determine acceptable flight conditions for UAS operations. Table 1 shows the relevant data sites for each river.

Table 1. Wave height, tidal, and meteorological data sources

Site Name	NDBC (Waves)	NOAA (Tides)	METAR (Winds)
Pajaro	46042 46114	9413450	KMRY
Carmel	46239	9413450	KMVI

C. UAS WAVE RUNUP OBSERVATION

Runup observation was conducted utilizing a small Commercial-Off-The-Shelf (COTS) UAS (Figure 5), small enough (<20lbs) to be categorized as Group 1 UAS under the DOD's UAS classification groups (Department of Defense, 2016). For Pajaro and Carmel, a DJI Inspire 1, with a Zenmuse X3 camera was utilized to conduct imagery collection. This camera provides a 20mm optical lens, 12.4M pixels, 94° Field-of-View (FoV), and up to 4096x2160 resolution. The total endurance for each flight was observed to be between 12–17 minutes dependent on the health of the batteries.

Figure 5. DJI Inspire 1 quadcopter

Each field day consisted of two-to-five individual wave runup collection videos, as well as an aerial mapping survey. Runup video times ranged between two-to-five minutes, with shorter two-to-three minutes videos to enable repositioning of the UAS in between videos and allow for several videos on the same flight. Consecutive shorter videos were also conducted as an accuracy check for the post-flight video processing, to ensure the ultimate runup positions for each transect were being found at the same

relative positions. Longer three-to-five-minute videos were conducted to allow for longer time series analysis.

Prior to launching the UAS, ground control points (GCPs) were placed on the beaches, and within the UAS FoV. A Spectra SP60 Global Navigation Satellite System (GNSS) receiver was used to map GCP locations by placing the receiver on each GCP square for at least six minutes to ensure a stable Global Positioning System (GPS) coordinate is attained. The GCP squares are spread out within the entire estimated FoV for the UAS, placing seven to nine for each flight. GCP locations were placed equally on both sides of the breach (if accessible), running both cross-shore and alongshore around the breach location. Specific location of GCPs was determined by providing ample vertical and horizontal spread and avoiding linear placement (Figure. 6). This was based on previous research with video imagery (Holland et al. 1997), observed stabilization results during initial collection post-processing, as well as verbal recommendations from oceanographic researchers at the U.S. Army Corp of Engineers, located in Duck, NC.

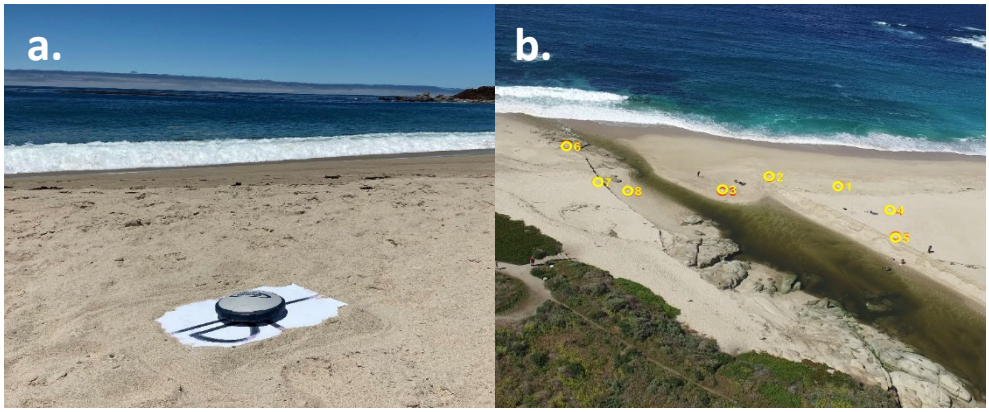

Figure 6. GNSS receiver mapping a GCP (a) and GCP spread (yellow circles) for UAS collection flight (b).

D. TOPOGRAPHIC AND BATHYMETRIC SURVEYS

Topographic surveys were conducted using both an aerial mapping survey from the UAS and a walking survey with the GNSS receiver mounted on a backpack, covering the desired observation area. For the walking surveys, height measurements were taken

for each researcher to adjust the end elevation data (Figure 7). Parallel transects across the subaerial region into the swash zone were utilized, with a roughly 10m-20m separation, to capture elevation changes as the sensor moved further away from the ocean. Each transect would end approximately calf deep water within the swash zone and shoreward far enough in to capture significant elevation changes that could affect both runup and river breaching dynamics. Additionally, each survey included walking the edge of both sides of the breach (if present and accessible) as well as the swash zone edge for approximately 50–100m in both directions from the breach.

Figure 7. GPS walking survey set up and antenna height measurement.

Bathymetric surveys were conducted using a Sontek River Surveyor M9 ADCP mounted on top of a Hydroboard with stabilizing fins attached to either side. To gather the depth data in the surf zone, a sit-on-top beach kayak was utilized to tow the sensor up to within 100m of the shoreline. A small outboard boat was used to tow the sensor, extending the survey out to around 200–400m from the shoreline.

E. DATA PROCESSING

UAS imagery was processed using the Coastal Imaging Research Network's (CIRN) Quantitative Coastal Imaging toolbox, with MATLAB (Palmsten and Brodie 2022). This toolbox takes coastal imagery and translates them from a three-dimensional space into a two-dimensional local cartesian field. These rectified images enable quantitative analysis of the coastal environment and specifically in the case of this research wave runup location. The toolbox enables the user to place cross-shore and along-shore transects at any location or length within the image space (Figure 8.a). The toolbox then generates pixeled time series images of the surf zone wave and swash zone extent along each transect from the rectified images. This dataset was then analyzed utilizing an edge detection function within MATLAB, developed in this study.

The function calculates the pixel intensity gradient from the CIRN time-stack imagery output (Figure 8.b) and plots an estimated time series of the position of the leading swash zone edge along the transect (Figure 8.c). The pixel intensity gradient is a function of distance for each vertical slice from the CIRN time-stack imagery. The edge detection method that worked best determined the location of maximum gradient on the land side of the instrument, which corresponded to a peak in pixel intensity at that location. This region of maximum intensity usually corresponded to where white foam edges were present. This algorithm worked well especially at Carmel owing to the good contrast with each individual wave. However, some observations at Pajaro suggest the algorithm could be adapted for regions where there are either offshore bars or poor wave contrast at the runup level.

From the swash zone edge, the value and local position relative to the transect, for the highest 2% extent of the runup ($R_{2\%}$) is calculated. The position values are then rotated back from the local cartesian coordinate system to world UTM coordinates, providing a geographic location for the $R_{2\%}$ value for each specific transect.

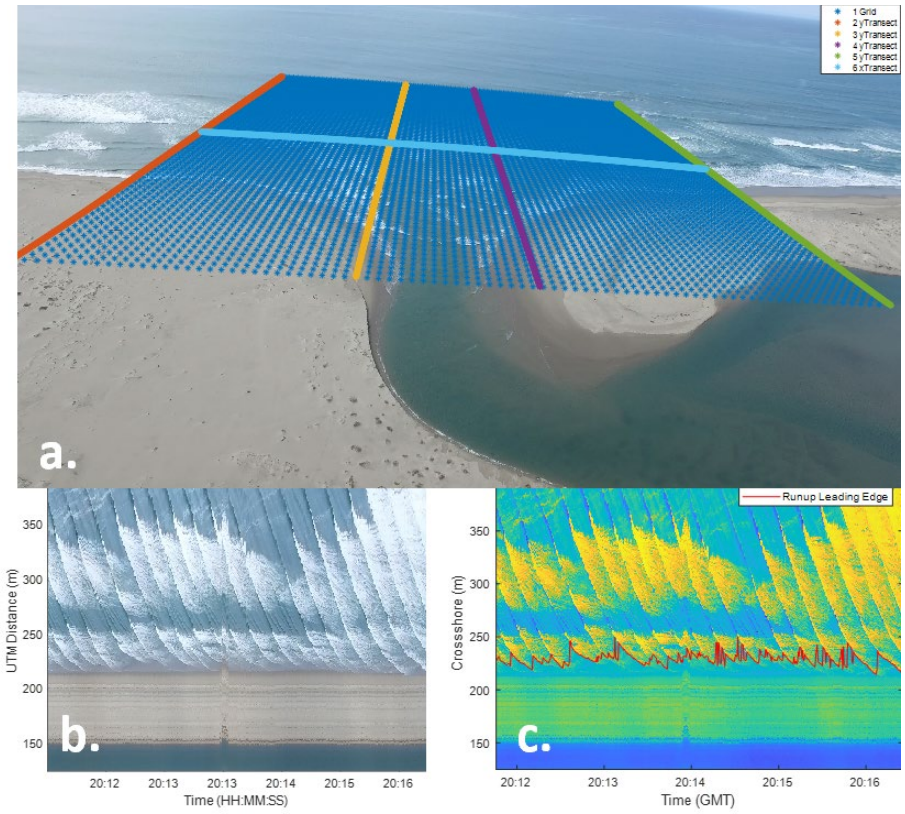

Figure 8. CIRN imagery output showing transect placement (a), wave propagation time series for a single transect (b), and edge detection output showing runup position relative to swash zone (c).

In addition to hovering wave runup collection, mapping surveys were conducted over the field sites. Imagery was also collected in a "mapping" mode using Pix4D with 80% overlap and a 75° camera angle and then processed via a photogrammetry process within Agisoft Metashape. This process produces 3-D spatial data enabling indirect measurements. Using their embedded software, a point cloud and digital terrain model (DTM) and digital elevation model (DEM) are derived from the uploaded imagery and GCP data, enabling the extraction of the survey region's three-dimensional structure. From this structure, the survey area's topography can be recreated. With the increased development of low-cost UAS, this methodology is being increasingly utilized to produce rapid and highly accurate surveys (Mokrane et al. 2019; Yang et al. 2020; Jiménez-Jiménez et al. 2021). The mapping survey images can also be stitched together, using the in-image GPS reference points. On this output, individual transects, $R_{2\%}$ locations, and

GCP points can be overlayed to provide a visual verification check of positional accuracy against overhead imagery (Figure 9).

Figure 9. Agisoft mapping survey imagery output.

The DEM, as well as the walking survey data, are then uploaded into the Aquaveo Surface-water Measuring Software (SMS) for comparison between different dates. The uploaded DEM structure, specifically elevation as it relates to specific geographic coordinates can then be directly compared and correlated to the data from the GPS walking survey. Geographic coordinates for the runup position for each video analysis are plotted against the DEM topographic structure built for that day to provide an initial elevation value for runup, referenced to the NAVD88 geodetic datum (Figure 10).

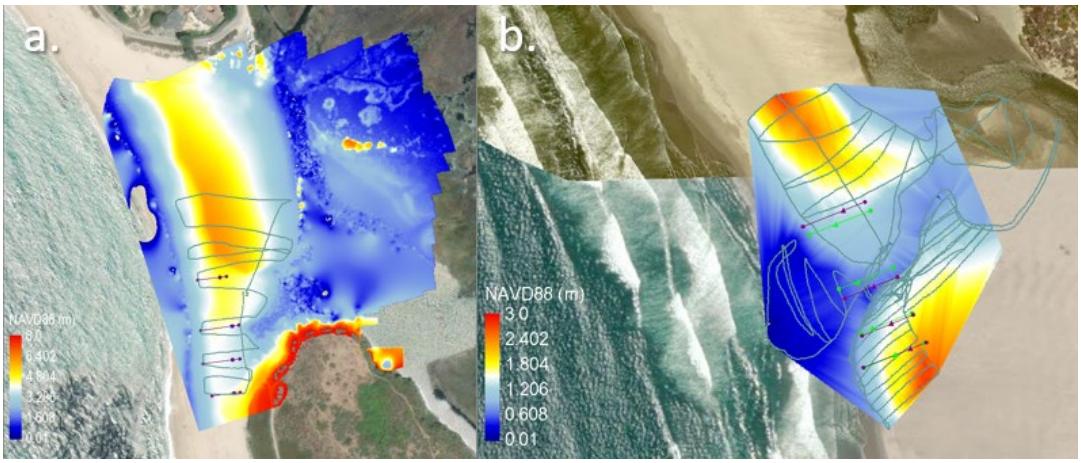

Figure 10. SMS DEMS output from Agisoft with walking survey (dark green line) and runup observation transects (purple and bright green) overlayed for Carmel River (a) and Pajaro River (b).

F. EMPIRICAL METHODS

Four empirical prevalent runup models were selected to conduct direct comparisons to observed runup values. The first model (2) is Hunt's (1959) formulation. Hunt's model continues to prevail as a foundation for all existing empirical runup models. The next two models were chosen based on Atkinson et al. (2017) conclusion on the increased accuracy of the Holman (1986) model (3) and the Vousdoukas et al. (2012) model (4). They conducted an accuracy assessment of eleven existing models against locally observed runup values from eleven beaches along the eastern Australia shoreline. The final model compared against was Stockdon et al. (2006), which is extensively cited in wave runup literature. This model has two formulations based on the reflectivity of the beach. For most natural beaches a model accounting for both setup and swash (5a) is provided. For highly dissipative beaches, runup was found to be best determined by a "dissipative-specific parameterization" (5b), which was based only on offshore wave conditions and not affected by the slope of the beach.

Empirical models are represented by

$$\frac{R}{H} = 2.3\ \frac{\beta}{\sqrt{H/T^2}} \tag{2}$$

$$R_{2\%} = 0.83\beta\sqrt{H_S L_p} + \ 0.2H_S \tag{3}$$

$$R_{2\%} = 0.53\beta\sqrt{H_S L_p} + .58\xi\sqrt{\frac{H_S^3}{L_0}} + .045 \tag{4}$$

$$R_{2\%} = 1.1\left(\frac{H_S L_p(0.563\beta+0.004)}{2} + 0.35\beta\sqrt{H_S L_p}\right), for\ \xi \geq 0.3 \tag{5a}$$

$$R_{2\%} = 0.043\sqrt{H_S L_p}\ \ for\ \xi < 0.3 \tag{5b}$$

with the parameter

$$L_0 = \frac{gT^2}{2\pi}\ . \tag{6}$$

Deep water wavelength and period are interdependent values linked by the linear dispersion relationship as shown in equation (6) (Stockdon et al. 2006). The Iribarren number is defined as shown previously in Equation (1) (Iribarren and Nogales 1949; Battjes 1974). β is defined as the cross-shore rise-over-run from the swash zone to the foreshore. Elevation data for each transect was attained via SMS DEMS output. To account for any variance in alongshore bathymetry due to river breach morphological impacts, the transect slope values were not averaged. Runup is comprised of two primary components, setup (η), which is the elevation of the mean sea level, and swash (S), which is the fluctuation of the water level above and below the setup (Guza and Thornton 1982; Atkinson et al. 2017; da Silva et al. 2020). To determine the runup value from the elevations plotted on SMS, the tidal signal was removed, as previous research by Vousdoukas et al. (2012) has shown a correlation between runup estimate error and tidal variations. Using NOAA observed water levels from the nearest tidal gauge at the closest measured observation times, water level deviation from NAVD88 was subtracted from the observed runup elevations for each transect. Each model was run against each transect individually, accounting for local slope variability, to create a broader and more precise dataset to compare the observations against. As each field collection period was on the

order of 20 to 40 minutes, the closest significant wave height and dominant wave period measurements to the middle of each video were utilized as model input values.

THIS PAGE INTENTIONALLY LEFT BLANK

IV. ANALYSIS AND RESULTS

A. TOPOGRAPHY AND BATHYMETRY

Visual observations of the foreshore beach slope and wave energy interaction at the Carmel River site shoreline are indicative of a mostly reflective beach. The wide spread of observed runup results indicate that it is not always the case and suggest that at certain locations and conditions the Carmel beach can also have dissipative characteristics. Previous wave studies at Carmel determined a standard β value of 0.10, or 10 cm/m (Laudier et al. 2011; Orescanin et al. 2018). Updated measurements showed a varying slope on the beach between 2–12 cm/m, in areas just north and south of the breaching region, with the largest slopes being found to the north (Figure 11). Factoring incoming wave dimensions, the corresponding Iribarren values equate to $0.18 \leq \xi \leq 1.3$, with a mean value of 0.70. This generally aligns well with the Stockdon (2006) parameterization of reflective beaches of $\xi \geq 0.3$. A 2020 study by Didier et al. introduced a more specific Iribarren breakout based on the evaluation by Stockdon, introducing an intermediate range, ($0.3 < \xi < 1.25$), and purely reflective beaches ($\xi \geq 1.3$). They proposed this range to account for swash "becoming saturated" and no longer being influenced by growing offshore wave heights and a portion of the wave energy is dissipated as incoming waves break. Using their delineation, Carmel would thus be classified as an intermediate beach, and classifying as purely reflective will likely result in an overestimation of runup values. The results presented here showed the opposite, with the models typically under-estimating the runup indicating that Carmel is a mostly reflective beach.

Due to the quick increase in water depth within the Carmel River surf zone, waves break very close to the shore (usually a single breaker at a time). Across the five observation days, surf zone widths ranged from 12–70m, with wider surf zones typically to the south of the breach region where there are prominent rocky outcrops that extend from the surf zone up onto the beach and promote wave breaking farther offshore (Figure 11).

Figure 11. Rocky portion of Carmel River to the south of breach.

Additionally, the northern section of the beach has larger and more consistent β values relative to south of the breaching region. Given that this was not a migratory year for the Carmel River, the northern section of the beach largely did not morphologically evolve (Orescanin et al. 2021). Runup was consistently higher along transects to the north. (Table 2). Due to the varying nature of the beach topography directly around the breach region between December 2021 and July 2022, northern transect values shown, are derived from transects at least 100m north of the northern most edge of the rocky swash zone that can be seen in Figure 11. Southern transect values are from any transect which was over the rocky region circled in Figure 11, not to include any that were placed at an active breach. Measurements showed a larger slope to the north, which coincided with larger $R_{02\%}$ values. A full table of all runup observations, β measurements, and wave characteristics for all collection periods is provided in Appendices 1 and 2. Appendices show four measurements at each time, reflecting the four transects utilized during each video, with the order listed at each time running from south to north.

Table 2. Carmel River southern and northern transect comparison

	South Transects	North Transects
β (avg)	0.058	0.079
ξ (avg)	0.548	0.743
$R_{O2\%}$	1.69m ≤ $R_{O2\%}$ ≤ 3.72m	2.79m ≤ $R_{O2\%}$ ≤ 4.20

The Pajaro River slope and observed incoming wave energy are mostly indicative of a dissipative beach. There is much less variation of the foreshore slope across the observation area, and the highest β value is observed to the south of the breaching region. Our observations from all the cross-shore transects, showed a varying slope between 1–6 cm/m, in areas just north and south of the breaching region (Figure 12). Factoring incoming wave dimensions, the overall Iribarren values equate to $0.004 \leq \xi \leq 0.990$, with the smallest values being those derived from directly at the breach. This aligns largely with the Stockdon (2006) parameterization of dissipative beaches of $\xi \leq 0.3$. An exception to this was south of the breach, where the beach slope was slightly larger which resulted in higher Iribarren values as well as larger observed runup values. The incoming wave energy south of the breach showed slight reflective characteristics, with an average ξ of 0.369, compared to the northern portion of the beach, with higher corresponding observed runup values and less observable alongshore directed swash.

Table 3. Pajaro River southern and northern transect comparison

	South Transects	North Transects
β (avg)	0.024	0.014
ξ (avg)	0.369	0.215
$R_{O2\%}$	-0.06m ≤ $R_{O2\%}$ ≤ 3.07m	-0.13m ≤ $R_{O2\%}$ ≤ 2.26m

Except for a single low tide observation, runup was always noted as higher to the south of the breach region. Of note, the negative runup values for the north and south were based on a single collection video at low tide. The breach runup measurements for that day also resulted in negative values; however, those measurements were taken of runup coming up the breach, where river outflow had cut through the beach.

Over the last five years (2017–2022), the breach site of the Pajaro River has meandered north and south over a total alongshore distance of approximately 1,000m. For the period of our collections from February 2022 to September 2022, the foreshore slope was observed to be highest to the south of the existing breach and relatively consistent from the region around the breach and to the north for several hundred meters.

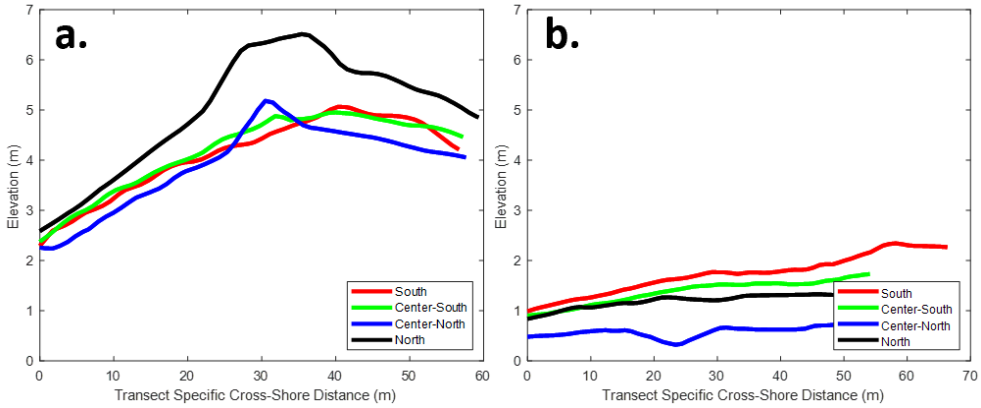

Figure 12. Foreshore transect slopes for Carmel River (03Dec21) (a), and Pajaro River (15Apr22) (b)

Bathymetry measurements at the two sites, shown in Figure 13, revealed that the Carmel River site surf zone water depth increases at a rate four times as fast as Pajaro, with measured β values of .045 over a 300m transect for Carmel, and .011 over a 1,000m transect for Pajaro. Referencing the wave conditions at the time of our observations, these β values correspond to Iribarren parameters of $0.3 \leq \xi \leq 0.49$ for Carmel and $0.14 \leq \xi \leq 0.19$ for Pajaro.

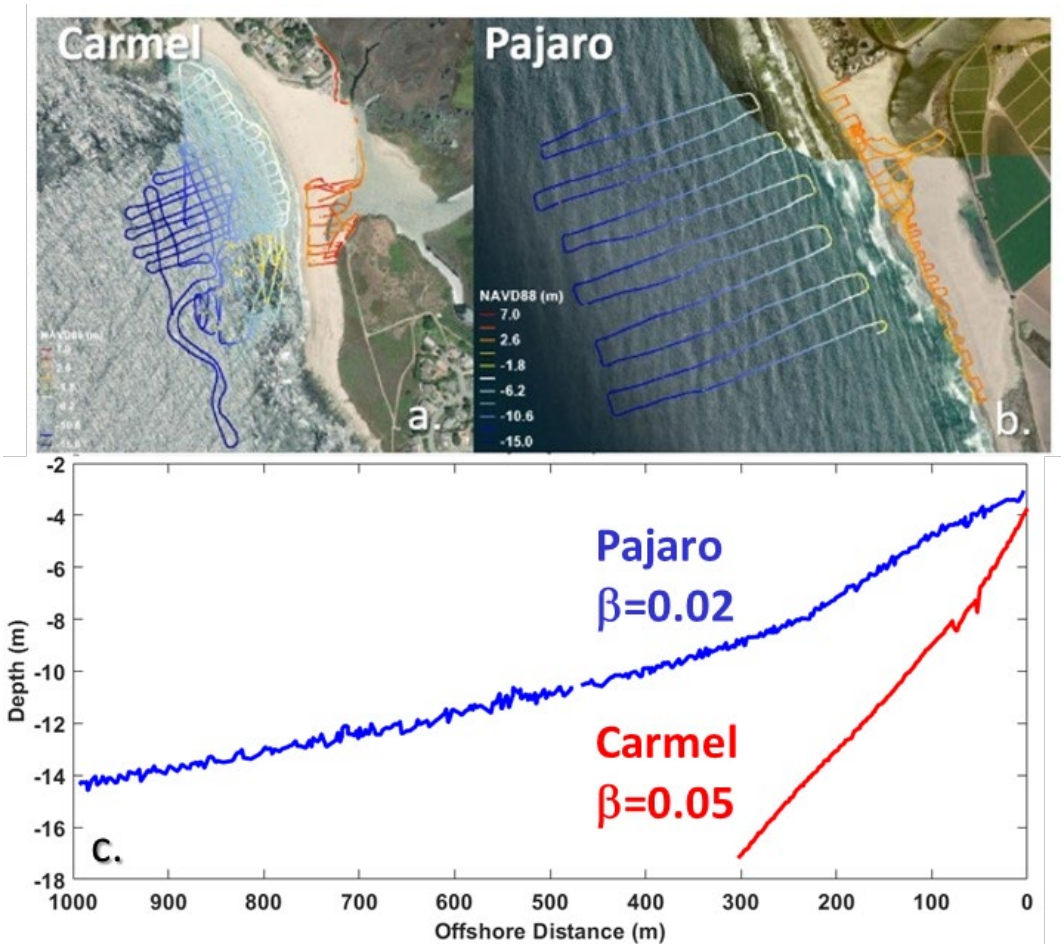

Figure 13. Bathymetry and topographic measurement surveys for the Carmel and Pajaro river sites, (a) and (b), respectively. Depth vs. distance bathymetry plot for both sites is shown in (c).

B. RUNUP OBSERVATIONS

Five separate collection periods were conducted at both the Carmel River and Pajaro River sites. The tidal conditions for the complete collection periods, across all videos for these days are reflected in Table 2.

Table 4. Collection dates, durations, tidal stage, and measured water levels

Field Site	Date	Total Collection Duration	Tidal Stage	Water Level (m) (NAVD88)
Carmel	03Dec21	36 min	Ebb	0.42 → 0.62
Carmel	14Jan22	11 min	Ebb	1.03
Carmel	10Mar22	27 min	Low	0.22
Carmel	15Jun22	10 min	Flood	0.71 → 0.75
Carmel	13Jul22	66 min	Ebb	1.23 → 1.13
Pajaro	18Feb22	22 min	High	1.50
Pajaro	11Mar22	26 min	Low	0.10
Pajaro	15Apr22	24 min	Ebb	1.02 → 0.90
Pajaro	15Jul22	31 min	Flood	1.00 → 1.14
Pajaro	30Sep22	50 min	High	1.72 → 1.75

Following the video and GPS processing, twenty-one total videos were utilized for data analysis, from seven different days—twelve from the Carmel River site, and nine from the Pajaro River site. Videos on three of the days (10 March, 15 July, 30 September) resulted in video footage that could not be analyzed. The GPS data on 10 March 2022 from Carmel River had a high level of fluctuation and error during the collection period resulting in an inability to geographically rectify the derived runup and transect locations. The videos from Pajaro on 15 July 2022 were unusable due to extremely low threshold values on the image frames that the edge detection program could not resolve. The videos on 30 September 2022 were unable to be used due to thick fog that moved into the area during the collection period. While the wave runup is visible in the videos, the resolution is too poor for the edge detection software to detect the leading edge of the swash zone.

As a visual reference the following sets of panel figures (14-21) represent a subset of the total imagery processed from each site and day. The top row for these figures depicts time series of wave runup for a single collection video, derived from three of the transects utilized. From left to right on the top row, the images reflect the wave data from south of the breach, a breach region, and north of the breach transects. The bottom row

for each figure depicts the runup edge detection (red line) for the time series directly above it.

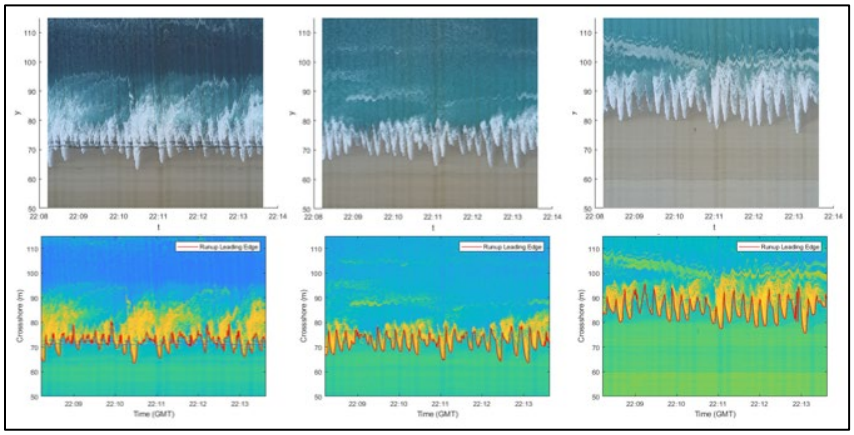

Figure 14. Carmel River observations for 03 December 2021

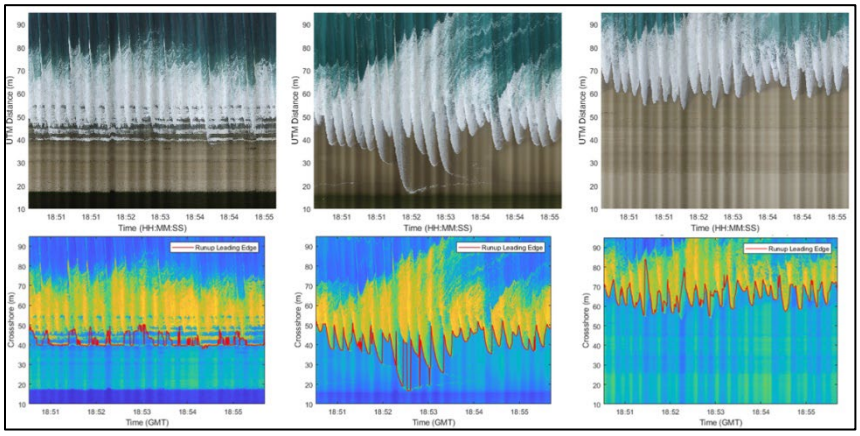

Figure 15. Carmel River observations for 15 January 2022

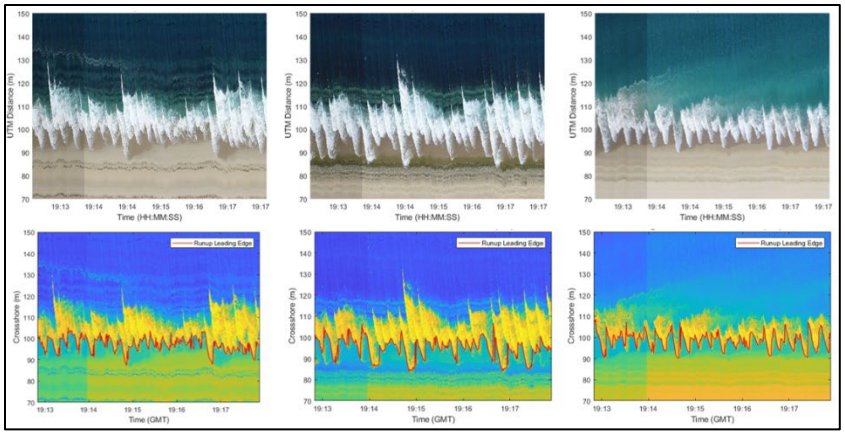

Figure 16. Carmel River observations for 10 March 2022

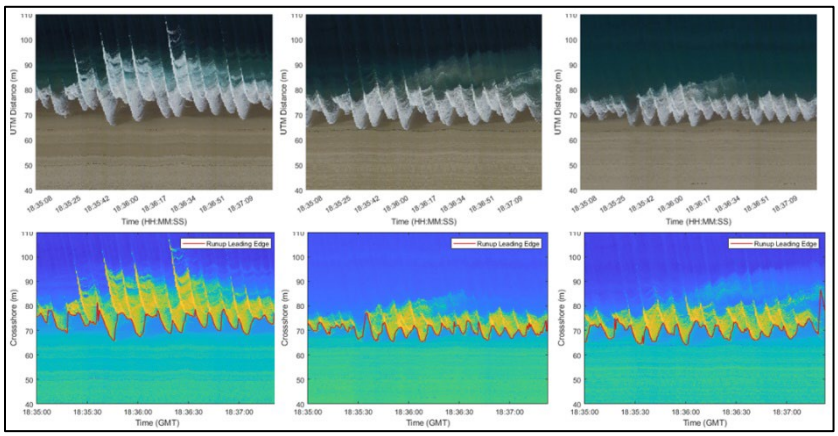

Figure 17. Carmel River observations for 15 June 2022

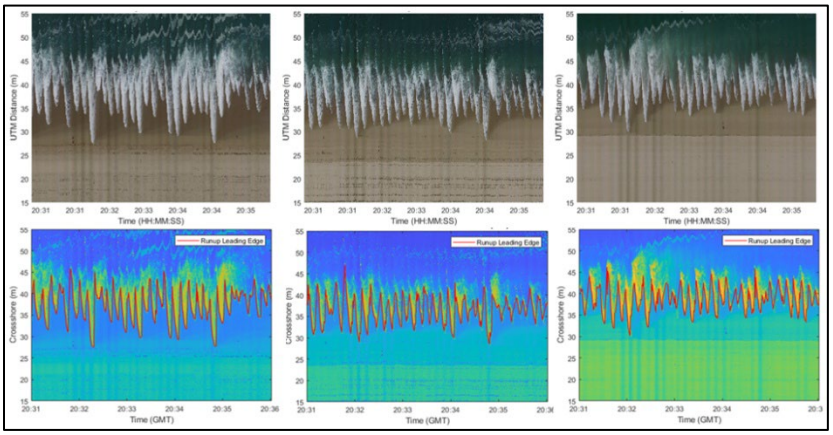

Figure 18. Carmel River observations for 13 July 2022

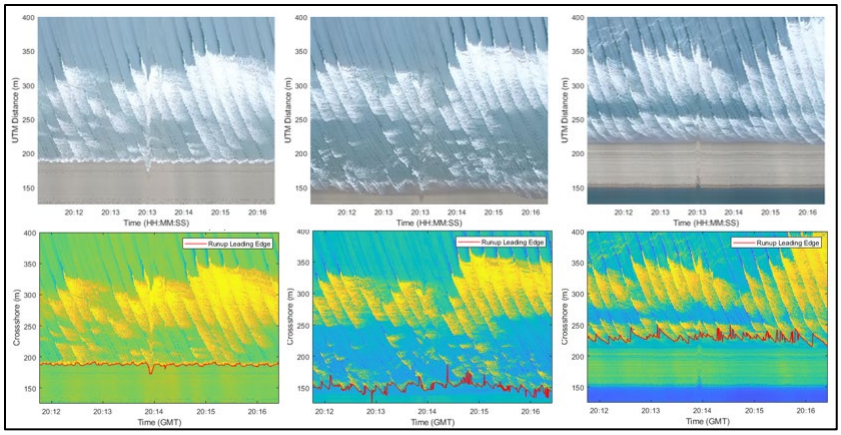

Figure 19. Pajaro River observations for 18 February 2022

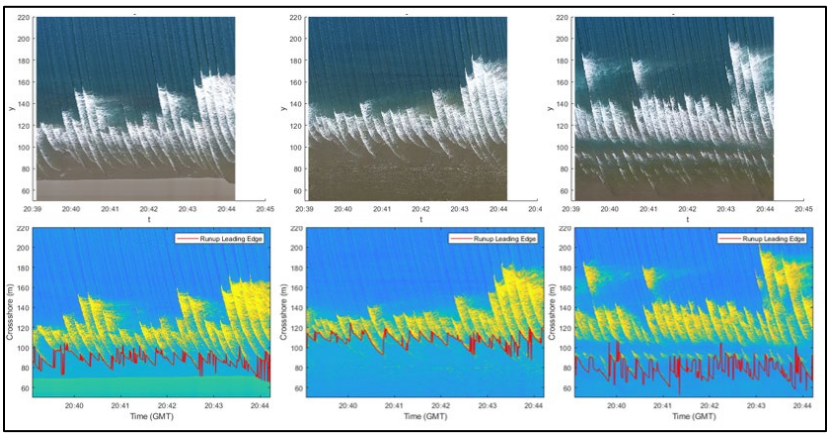

Figure 20. Pajaro River observations for 11 March 2022

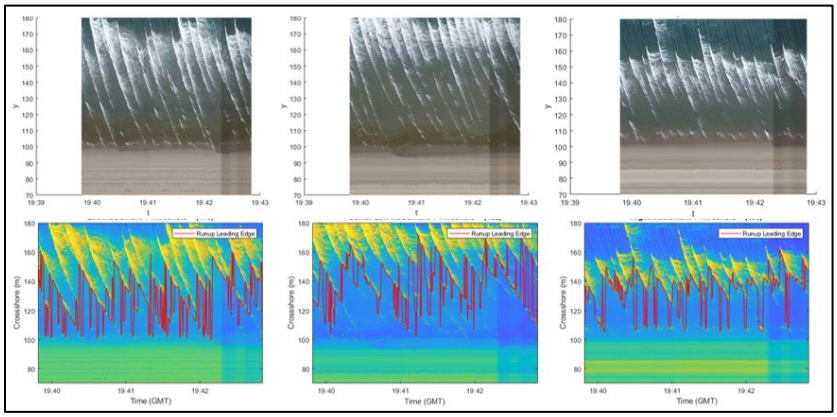

Figure 21. Pajaro River observations for 15 April 2022

Runup values ($R_{2\%}$) from all collected observations and associated model outputs were plotted to assess the overall spread of the data from each site, along with a separate linear regression of observation values ($R_{O2\%}$) and output from the empirical models ($R_{M2\%}$) listed in Section III.F. These results are shown in Figures 22 and 23. Box plots in these two figures indicate the inner quartile data range (Q_3–Q_1), with the red line designating the median value and the whiskers showing the maximum and minimum data extent. Tables 5 and 6 list the Pierson Correlation Coefficients (r) (8) and covariance (σ_{xy}) (9) values of the $R_{O2\%}$ regression to the corresponding $R_{M2\%}$ output values for Carmel and Pajaro. The Pierson Correlation Coefficient ranges from -1.0 to +1.0, showing a positive or negative correlation, and is dependent on the strength of the linear relationship between the observations and model outputs. Covariance is measured to show how the observations and model output vary in relation to their expected values and how they will move in relation to each other. Covariance values are not indicative of the strength of the relationship between the observations and the model output, which are all independent of each other.

$$r = \frac{\sum(x_i - \bar{x})(y_i - \bar{y})}{\sqrt{\sum(x_i - \bar{x})^2 \sum(y_i - \bar{y})^2}} \tag{8}$$

$$\sigma_{xy} = \frac{\sum(x_i - \bar{x})(y_i - \bar{y})}{N - 1} \tag{9}$$

For Pajaro analysis, Equation 5b was included in the analysis due to the dissipative nature of the Pajaro site. To assess any possible variance in the local topography changes, and breach impacts for each site, regressions were run in four groupings: the entire data set, north of the breach region, south of the breach region, and at or immediately next to the breach area.

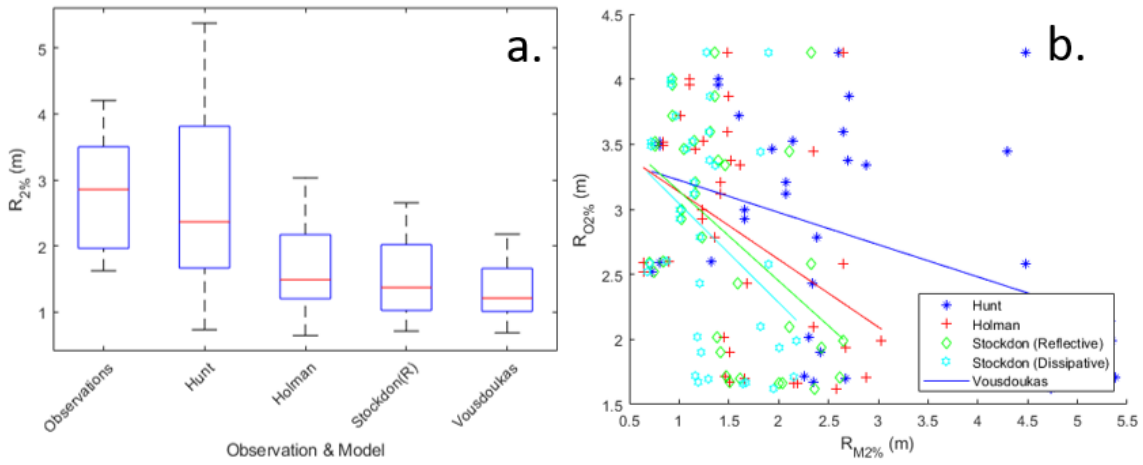

Figure 22. Carmel River $R_{O2\%}$ observed values (a) and $R_{O2\%}$ regression to $R_{M2\%}$ (b)

Table 5. Carmel River r and σ_{xy} values for observations and model output by transect location relative to breach

	All Transects		South Transects		North Transects		Breach Transects	
Model	**r**	**$\sigma_{x,y}$**	**r**	**$\sigma_{x,y}$**	**r**	**$\sigma_{x,y}$**	**r**	**$\sigma_{x,y}$**
Hunt	-0.392	-0.445	-0.574	-0.658	-0.606	-0.842	-0.368	-0.352
Holman	-0.400	-0.221	-0.566	-0.323	-0.351	-0.351	-0.427	-0.201
Stockdon (R)	-0.471	-0.231	-0.644	-0.321	-0.563	-0.345	-0.509	-0.212
Vousdoukas	-0.380	-0.137	-0.562	-0.205	-0.590	-0.257	-0.357	-0.109

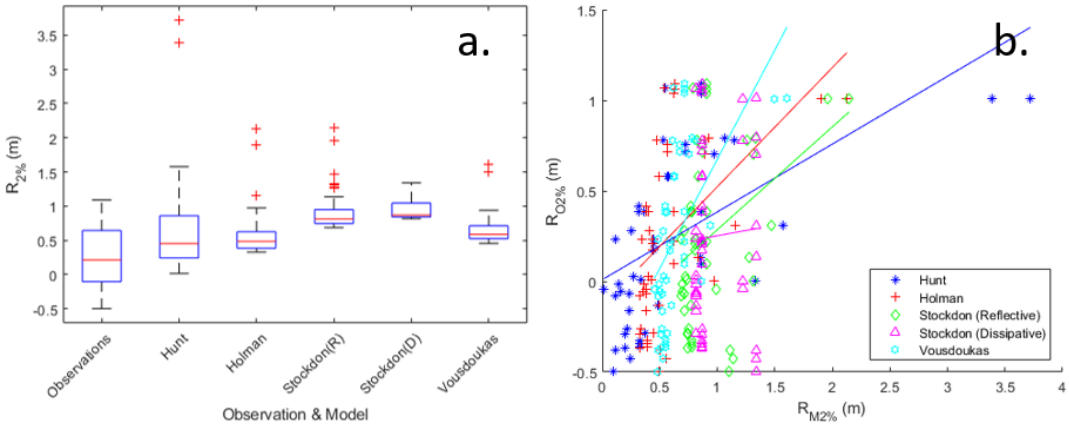

Figure 23. Pajaro River $R_{O2\%}$ values (a) and $R_{O2\%}$ regression to $R_{M2\%}$ (b)

Table 6. Pajaro River r and σ_{xy} values for observations and model output by transect location relative to breach

	All Transects		South Transects		North Transects		Breach Transects	
Model	**r**	**$\sigma_{x,y}$**	**r**	**$\sigma_{x,y}$**	**r**	**$\sigma_{x,y}$**	**r**	**$\sigma_{x,y}$**
Hunt	.0562	0.188	0.546	0.265	-0.137	-0.018	0.770	0.102
Holman	0.497	0.084	0.503	0.122	-0.137	.0.011	0.669	0.044
Stockdon (R)	0.372	0.054	0.498	0.099	-0.183	-0.015	0.322	0.025
Stockdon (D)	0.049	0.005	0.383	0.032	-0.205	-0.013	0.003	0.00
Vousdoukas	0.560	0.058	0.544	0.082	-0.134	-0.005	0.771	0.032

For the Carmel River site, there was very poor correlation between the observations and the predicted output across all the models. $R_{O2\%}$ values were significantly higher than all the $R_{M2\%}$ output. Additionally, the variance between values grew, with larger $R_{O2\%}$ values correlating to lower $R_{M2\%}$ values and vice versa. This growth in variance was lowest with the Vousdoukas model. The Pajaro site demonstrated better correlation between the observations and the models. The inverse relationship observed at Carmel was not observed at Pajaro. Higher $R_{O2\%}$ values corresponded reasonably well to higher $R_{M2\%}$ values, specifically when assessing the Vousdoukas model.

As the Iribarren value has been widely shown to have a strong correlation to wave runup, a regression of $R_{O2\%}$ and $R_{M2\%}$ to the Iribarren number was conducted to determine the magnitude of the Iribarren value's importance to both the individual models' output, as well as runup observations (Figure 21). The associated coefficient of determination values (R^2) (10) is provided in Tables 5 and 6.

$$R^2 = \frac{\sum_m \sum_n (A_{mn} - \bar{A})(B_{mn} - \bar{B})}{\sqrt{\sum_m \sum_n (A_{mn} - \bar{A})^2 (B_{mn} - \bar{B})^2}} \qquad (10)$$

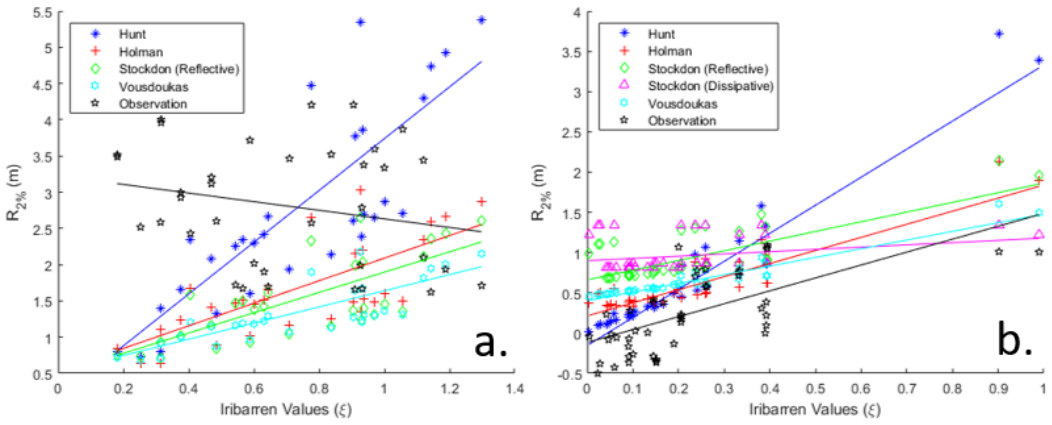

Figure 24. $R_{O2\%}$ and $R_{M2\%}$ regression to ξ for Carmel (a) and Pajaro (b) rivers

Table 7. R^2 values for Carmel River $R_{2\%}$ to ξ regression

Model	All Transects	South Transects	North Transects	Breach Transects
Hunt	0.839	0.853	0.8456	0.794
Holman	0.752	0.776	0.763	0.685
Stockdon (R)	0.7624	0.787	0.795	0.691
Vousdouskas	0.829	0.845	0.834	0.780
Observations	0.221	0.436	0.783	0.035

Table 8. R^2 values for Pajaro River $R_{2\%}$ to ξ regression

Model	All Transects	South Transects	North Transects	Breach Transects
Hunt	0.950	0.964	0.953	0.924
Holman	0.881	0.936	0.898	0.660
Stockdon (R)	0.751	0.910	0.852	0.225
Stockdon (D)	0.271	0.671	0.744	0.185
Vousdouskas	0.948	0.963	0.951	0.920
Observations	0.656	0.694	0.145	0.685

As the Iribarren number is parameterized based on both β and wave characteristics, and the bathymetry is significantly different between the two sites, a comparison of runup to those specific factors was conducted. Tables 7–10 show the statistical data for the $R_{O2\%}$ & $R_{M2\%}$ values regressed to both beach slope and wave height.

Table 9. R^2 values for Carmel River $R_{2\%}$ to H_S regression

Model	All Transects	South Transects	North Transects	Breach Transects
Hunt	0.374	0.504	0.337	0.366
Holman	0.510	0.622	0.466	0.521
Stockdon (R)	0.475	0.583	0.420	0.486
Vousdouskas	0.393	0.518	0.358	0.388
Observations	0.222	0.280	0.288	0.484

Table 10. R^2 values for Pajaro River $R_{2\%}$ to H_S regression

Model	All Transects	South Transects	North Transects	Breach Transects
Hunt	0.377	0.663	0.860	0.062
Holman	0.559	0.737	0.930	0.436
Stockdon (R)	0.731	0.790	0.931	0.794
Stockdon (D)	0.934	0.934	0.934	0.934
Vousdouskas	0.381	0.666	0.863	0.056
Observations	0.027	0.068	0.121	0.052

Table 11. R^2 values for Carmel River $R_{2\%}$ to β regression

Model	All Transects	South Transects	North Transects	Breach Transects
Hunt	0.850	0.889	0.882	0.793
Holman	0.782	0.829	0.809	0.711
Stockdon (R)	0.757	0.818	0.836	0.658
Vousdouskas	0.848	0.886	0.872	0.794
Observations	0.079	0.313	0.705	0.184

Table 12. R^2 values for Pajaro River $R_{2\%}$ to β regression

Model	All Transects	South Transects	North Transects	Breach Transects
Hunt	0.979	0.9877	0.974	0.956
Holman	0.926	0.968	0.943	0.719
Stockdon (R)	0.800	0.946	0.871	0.270
Stockdon (D)	0.325	0.722	0.761	0.149
Vousdouskas	0.978	0.987	0.974	0.954
Observations	0.636	0.637	0.084	0.724

No significant correlation was found between the runup data and wave heights at either site; however, there was strong correlation between model output runup and beach slope, specifically at Pajaro. Where this is acutely apparent is in the reduction in R^2 values for calculations and measurements at the breach. Both north and south of the breach, bathymetry is relatively uniform moving offshore and experiences minimal change over short periods. At the breach, however, there is increased variability across observation periods due to the impacts of river discharge and shifting the beach profile between the lagoon and the ocean. Two conditions worth mentioning, that likely cause the improved correlation to β at Pajaro than Carmel, are bathymetric differences, both north to south and between the surf zone and the foreshore, and bottom sediment type.

C. RESULTS SUMMARY

Image processing showed high accuracy and precision across all Carmel videos, due to the narrow swash width, and lack of multiple wave lines within each individual time series, as previously shown in Figures 14–18. Non-uniformity of β values from north to south, result in low r values (Equation 8) when comparing the model outputs to observed runup values. Assessing R^2 (Equation 10) indicated high correlation between model runup output with ξ values. Further correlation analysis shows this is

predominantly due to the β influence as compared to the influence of offshore wave characteristics. Runup observations, in general, showed low R^2 with both β and Hs values.

Pajaro had more instances of image processing and edge detection error, which contributed to higher overall scatter and error in the observed runup values relative to Carmel. Analysis of r and R^2 values for Pajaro show a similar trend as Carmel, with higher runup (model output and observation) correlation to β than with offshore wave characteristics, even with the smaller overall slope.

THIS PAGE INTENTIONALLY LEFT BLANK

V. DISCUSSION

A. EMPIRICAL MODEL OBSERVATIONS

Analysis of the observations and model outputs at both sites, showed a stronger overall positive correlation at Pajaro as compared to Carmel. An inverse relation, from what was expected between observations and model output values, was observed from the Carmel River data as shown in Figure 22 and Table 5. As previously mentioned, Carmel morphology is much more varied, with changing bottom type, variable beach slope, and larger effects by wave refraction. The models utilized for reference in this study are largely for natural, gently sloping, reflective, uniform beaches and do not account for micro-scale variance from the conditions just listed. Da Silva (2020) talks in detail about the benefit of the need to use "additional and more complex parameters" to better account for the various processes and conditions that affect runup as it moves up the beach. The observations at Carmel showed a widespread in runup levels, indicating that attempting to apply a singular model at that site, will lead to significant error in runup estimations.

The Stockdon reflective model (Equation 4), is an exception to the overall better performance at Pajaro, showing lower overall skill compared to the other models. This is not surprising as Pajaro has generally dissipative characteristics ($\xi<0.3$) for large portions of the beach. The one region of Pajaro where this was observed to not be the case, is to the south of the breach location. Stockdon's reflective model runup shows approximately 63% improvement south of the breach, relative to measurements taken to the north. This correlates to an increase in ξ between the two areas, as shown in Table 3, from an average of 0.215 to an average of 0.369. This indicates that for areas south of the breach, the beach acts as a more reflective shoreline, and is backed up by the significantly higher performance of all the models for southern observations.

B. SOURCES OF ERROR AND POTENTIAL REMEDIES

Upon processing the collected imagery and evaluating the resulting data, several key sources of error were apparent and should be rectified or accounted for during future

collections. The beach at Carmel River has multiple bottom types, consisting of permeable (sediment) and impermeable (rocky) surfaces, each of which effect wave runup differently. To the south, there is an observable rocky bottom that is not present to the north, which has a smooth sandy bottom and steeper foreshore. A recent thesis study in South Africa, by Holländer (2022), looked at the specific shortfall of existing models in relation to bottom roughness and proposed incorporating a "roughness influence" factor for beaches with impermeable bottom types, with promising but limited results.

Additionally, in the region around which the river typically breaches, the beach slope undergoes significant change from both natural and artificial influences. During the rainy season, when the river undergoes multiple breaches, the berm is naturally broken down, with sediment in that area being transported into the bay. Measurements from December 2021 to July 2022, showed the β value at the Carmel River breach region reducing from 7cm/m to 3cm/m. During this period there were two observed natural breaches in January and March, as well as artificial dredging of the breach area in the late Spring. The magnitude of these breaches, relative direction of the outflow, and incident angle of the incoming wave energy, determine the direction of outgoing river plume and location of eventual sediment deposits. This, over time, can affect the surf zone bathymetry.

Thermal imagery collected using a DJI Zenmuse XT infrared camera during these breaches showed the outflow, with its associated river plume, being trapped immediately near the breach site, or transported alongshore to the south (Figures 25 and 26). Temperatures in these images are relative, with brighter (white) shades indicating warmer temperature and darker (black) indicating colder temperature. At Pajaro, where the river tends to remain breached from late winter until late Summer, the only observation day where a breach was not occurring was on 30 September 2022. For all collection periods at Pajaro, the incoming wave energy was near normal to the shoreline, and direction of the outgoing river plume was primarily influenced by the orientation of the river mouth, and the balance of forces between incoming tidal energy and outgoing river velocity (Figure 26).

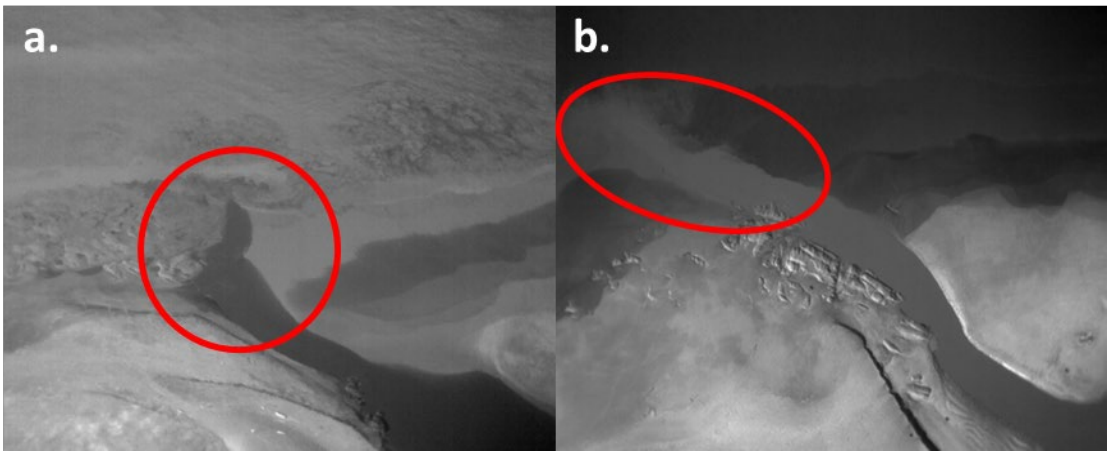

Figure 25. Outgoing Carmel River plume on 14 January 2022 (a) and 10 March 2022 (b)

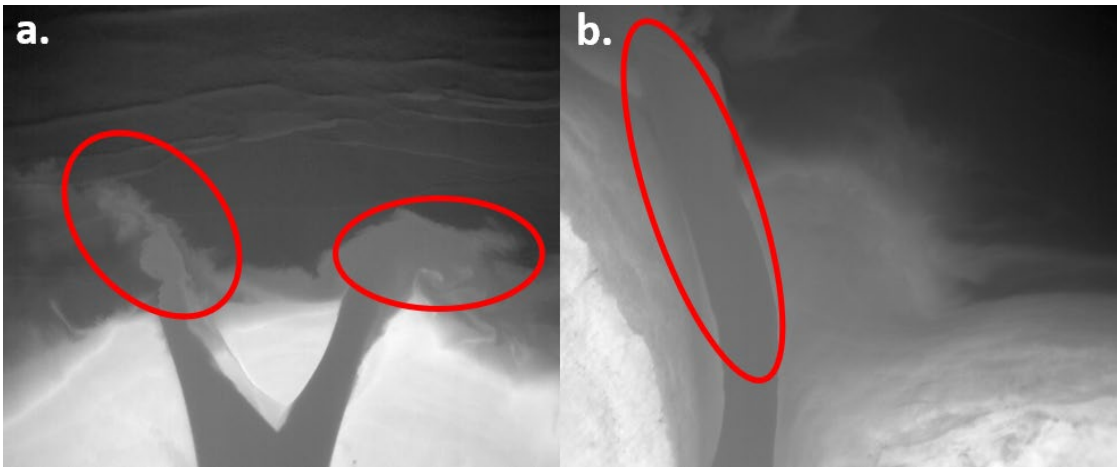

Figure 26. Outgoing Pajaro River plume on 11 March 2022 (a) and 15 April 2022 (b)

The second source of error stemmed from altering the UAS FoV between video captures on the same field day. This resulted in inconsistent geographic placement of the runup transects from video to video, during the image processing phase. Changing the drone's position and altitude was done to test accuracy of the imagery process and ultimate runup calculation and geographic positioning. However, due to the large variations in slope at the Carmel River site, inconsistency in transect placement resulted in small datasets at consistent areas, with which to compare against the model outputs. Ultimately, it was determined that ensuring accuracy of runup's geographic placement,

was less reliant on UAS altitude and more on being able to clearly identify and having sufficient GCPs and SCPs spread out in as broad a manner as possible within the UAS FoV. An additional transect-related error was associated with those that were placed immediately at or near the breach, specifically for Pajaro. Walking surveys were always done to capture the edges of the breach but often were not able to capture the dramatic drop when a breach wall was present, specifically at high tide, when the breach was substantially deeper. This resulted in some cross-shore error with the β values for transects in those specific areas. Additionally, due to the dynamic interaction between the outgoing river flow and the incoming wave and tide energy, swash action was often confused, which resulted in alongshore propagation of the swash leading edge and distorting of where the runup was located within the image.

The third significant source of error was associated with the SCPs, and how the processing software was able to differentiate between the SCP square and the sand immediately surrounding it. SCPs were selected from the field of GCPs, as their elevation values were known. These squares were thick, all white poster board, roughly 60cm by 60cm. On days where ambient light fluctuated periodically, due to shadows from clouds passing overhead or from fog, the processing toolbox had difficulty maintaining a lock on the SCPs. This can be fixed by utilizing larger SCPs, and by incorporating a thick black border around the white, to create a more distinct threshold contrast for the software to detect.

The fourth source of error was associated with the GNSS receiver. This was encountered on a single collection day, 10 March 2022, at Carmel River, when a large amount of horizontal and vertical error was found within the GPS data. Due to this data not being visible until it is downloaded and processed, after leaving the field, there is little that can be done to overcome this issue in the field. This was a one-time problem but resulted in the inability to process all of the videos from one of only two observed breaches at Carmel River, with horizontal error on the order of several hundred meters, and vertical error on the order of approximately a meter.

The final source of error was related to a combination of the edge detection function's ability to consistently capture the true leading edge of the runup, coupled with

SMS image resolution (1m by 1m). Quantification of the error associated with the horizontal extent of runup was not able to be precisely derived, however, was assumed to be small based on visual verification of plotted geographic runup locations, relative to overhead imagery, and consistency of runup locations when compared across all four transects at the same time. For Carmel, the horizontal geographic error was determined to be negligible (<1m), and for Pajaro, an approximated range of 2–5m was determined. Based on β values along each transect, and the SMS image resolution, this results in a vertical error bar estimation around the observed runup values of 50cm.

C. DECREASING THE HUMAN FOOTPRINT

Through the overall process conducted in this research, there was still a significant need for a person to be physically present on the beach. Objectively, to enhance applicability for the U.S. Navy, that needs to be reduced. There are two key steps that could be modified for future work. The first is leveraging the large accuracy improvement with UAS internal GPS hardware. This can be leveraged by attaining the beach topography elevation, via the aerial mapping surveys (using Structure-from-Motion), in place of the walking surveys. This methodology was demonstrated by Young (2018) and Coughlin (2019). During this study, walking survey data was chosen over the aerial survey method due to an observed small improvement in vertical accuracy between the two methods, and for consistency of methods, as aerial mapping surveys were not done on every collection day due to changing flight conditions throughout the collection period. Walking surveys immediately around the breach areas for each site typically took between sixty to ninety minutes. The UAS was able to survey areas three to five times that area in fifteen to twenty minutes, with a general variance in vertical accuracy of less than 0.2m

The second is mapping the images to geographic coordinates. Artificial ground control points were leveraged extensively for this study, however, with the improvement of UAS internal GPS systems, this requirement could be reduced or modified. A key component of a GCP is knowing exactly where it resides in world coordinates. If a surveyor can leverage multiple known, geographically accurate natural or permanent

man-made features that are spread out within the FoV, this could reduce or even remove the need for artificial GCPs. A 2017 work by Holman et al. specifically looked at this, demonstrating the ability with just four known points, and utilizing the UAS internal GPS data, to attain horizontal accuracy from rectified images to within 0.21m

VI. CONCLUSION

UAS imagery-derived runup estimates were attained from two separate beaches with dissimilar morphological properties over ten observation periods. Runup observations were compared to a series of commonly cited empirical runup models to ascertain the accuracy of these models at two beaches with non-uniform features. Runup was shown to be affected by each beach's morphological variations which resulted in a significant vertical runup range within small alongshore distances. Existing models did not demonstrate meaningful skill in accounting for this variance, as they only account for the core parameters of foreshore beach slope and offshore wave characteristics. Empirical models have been shown to work reasonably well for long, straight natural beaches which have small to no nearshore features, which would impact incoming wave energy. The results at the southern portion of Pajaro are in relatively good agreement with these models and reflect the dominance of these parameters when no other influences are present. Carmel River and the northern portion of Pajaro highlighted the shortfall of utilizing any model without accounting for the differences in the surf zone bathymetry and bottom type. The rocky bottom in the southern part of the Carmel River survey location clearly affected the incoming wave runup, especially within the swash zone, diffusing much of the wave energy in a confused manner that the models could not accurately predict.

The slope at Carmel accounted for two distinct impacts on incoming wave energy. Overall beach slope for the transects varied from 2 cm/m to 11 cm/m across a limited 200m alongshore distance. Cross-shore beach slope changed between the foreshore and the surf zone for certain locations along the beach, limiting the accuracy of applying a singular existing empirical model. There are models that differentiate between the different slopes by using the slope at the wave breaking point vice the foreshore slope, but to my knowledge none that account for a changing β value between the surf and swash zone. Carmel is also a more sheltered beach relative to the long straight shoreline present at Pajaro and other beaches utilized for many of the previous studies. The effect

of wave refraction, bathymetry changes, shoreline concavity all can play a part in how wave energy ultimately moves up the beach.

The Navy must be able to conduct operations in the littoral regions of the world where timely and accurate wave data and beach morphology are not typically readily available.Relying exclusively on existing runup empirical models or more modern graphical numerical models can induce significant errors in nearshore quantification. Poor data in almost always equates to poor results out. Errors or mischaracterizations of the nearshore environment directly contribute to unnecessary and increased risk to personnel and equipment. The utilization of small UAS can provide an instantaneous snapshot of the nearshore environment and specifically wave runup characteristics to operational planners, increasing the accuracy and precision of nearshore environmental characterizations. Maximizing this technology will directly reduce risk to Naval Forces and enhance our Navy's operational amphibious capability and effectiveness within the littoral regions. As the Secretary of the Navy recently stated in an August 2022 speech to Naval Postgraduate School students and faculty, "It's time to stop treating UAS as an emerging technology and instead utilize it as the established technology that it is" (Del Toro 2022).

APPENDIX A. CARMEL RUNUP DATA

Date/Time (GMT)	Observed Runup(- tide level) (m, NAVD88)	Beta (β)	Wave Height (Hs) (m)	Wave Length (Ls) (m)	Tidal Stage
12/3/21 21:10	1.90	0.062	2.08	215.71	Ebb
12/3/21 21:10	2.02	0.059	2.08	215.71	Ebb
12/3/21 21:10	2.10	0.110	2.08	215.71	Ebb
12/3/21 21:10	3.44	0.110	2.08	215.71	Ebb
12/3/21 21:40	1.69	0.058	2.25	277.14	Ebb
12/3/21 21:40	1.67	0.051	2.25	277.14	Ebb
12/3/21 21:40	1.72	0.049	2.25	277.14	Ebb
12/3/21 21:40	1.94	0.107	2.25	277.14	Ebb
12/3/21 21:48	1.67	0.084	2.25	277.14	Ebb
12/3/21 21:48	1.66	0.082	2.25	277.14	Ebb
12/3/21 21:48	1.62	0.103	2.25	277.14	Ebb
12/3/21 21:48	1.71	0.117	2.25	277.14	Ebb
1/14/22 18:53	2.58	0.088	3.13	243.71	Flood
1/14/22 18:53	1.99	0.105	3.13	243.71	Flood
1/14/22 18:53	2.43	0.046	3.13	243.71	Flood
1/14/22 18:53	4.20	0.088	3.13	243.71	Flood
6/15/22 17:32	3.52	0.027	2.4	108.23	Flood
6/15/22 17:32	3.00	0.056	2.4	108.23	Flood
6/15/22 17:32	3.21	0.070	2.4	108.23	Flood
6/15/22 17:32	4.00	0.047	2.4	108.23	Flood
6/15/22 17:37	3.49	0.027	2.4	108.23	Flood
6/15/22 17:37	2.93	0.056	2.4	108.23	Flood
6/15/22 17:37	3.12	0.070	2.4	108.23	Flood
6/15/22 17:37	3.96	0.047	2.4	108.23	Flood
7/13/22 19:35	3.52	0.080	1.39	152.25	Ebb
7/13/22 19:35	2.59	0.030	1.39	152.25	Ebb
7/13/22 19:35	3.87	0.101	1.39	152.25	Ebb
7/13/22 19:35	2.79	0.089	1.39	152.25	Ebb
7/13/22 19:57	2.52	0.024	1.56	172.94	Ebb
7/13/22 19:57	3.38	0.089	1.56	172.94	Ebb
7/13/22 19:57	4.21	0.086	1.56	172.94	Ebb
7/13/22 19:57	3.34	0.095	1.56	172.94	Ebb
7/13/22 20:34	3.72	0.063	1.48	128.88	Ebb
7/13/22 20:34	2.60	0.052	1.48	128.88	Ebb
7/13/22 20:34	3.60	0.104	1.48	128.88	Ebb
7/13/22 20:34	3.46	0.076	1.48	128.88	Ebb

THIS PAGE INTENTIONALLY LEFT BLANK

APPENDIX B. PAJARO RUNUP DATA

Date/Time (GMT)	Observed Runup (- tide level) (m, NAVD88)	Beta (β)	Wave Height (Hs) (m)	Wave Length (Ls) (m)	Tidal Stage
2/18/22 20:10	1.01	0.065	1.86	433.43	High
2/18/22 20:10	0.78	0.021	1.86	433.43	High
2/18/22 20:10	-0.04	0.001	1.86	433.43	High
2/18/22 20:10	0.00	0.026	1.86	433.43	High
2/18/22 20:14	1.01	0.065	2.24	433.43	High
2/18/22 20:14	0.79	0.019	2.24	433.43	High
2/18/22 20:14	-0.50	0.002	2.24	433.43	High
2/18/22 20:14	0.31	0.028	2.24	433.43	High
2/18/22 20:22	0.70	0.017	2.24	433.43	High
2/18/22 20:22	-0.43	0.004	2.24	433.43	High
2/18/22 20:22	-0.38	0.002	2.24	433.43	High
2/18/22 20:22	0.13	0.015	2.24	433.43	High
3/11/22 20:42	0.03	0.008	1.39	259.553	Low
3/11/22 20:42	-0.07	0.007	1.39	259.553	Low
3/11/22 20:42	-0.08	0.003	1.39	259.553	Low
3/11/22 20:42	0.01	0.010	1.39	259.553	Low
3/11/22 20:47	-0.06	0.005	1.39	259.553	Low
3/11/22 20:47	-0.16	0.007	1.39	259.553	Low
3/11/22 20:47	-0.29	0.011	1.39	259.553	Low
3/11/22 20:47	-0.13	0.014	1.39	259.553	Low
3/11/22 21:04	0.23	0.003	1.48	243.706	Low
3/11/22 21:04	-0.01	0.004	1.48	243.706	Low
3/11/22 21:04	0.28	0.007	1.48	243.706	Low
3/11/22 21:04	1.07	0.016	1.48	243.706	Low
4/15/22 19:38	0.72	0.012	1.19	342.103	Ebb
4/15/22 19:38	0.10	0.023	1.19	342.103	Ebb
4/15/22 19:38	-0.36	0.009	1.19	342.103	Ebb
4/15/22 19:38	0.17	0.012	1.19	342.103	Ebb
4/15/22 19:44	0.75	0.020	1.19	342.103	Ebb
4/15/22 19:44	0.22	0.023	1.19	342.103	Ebb
4/15/22 19:44	-0.35	0.009	1.19	342.103	Ebb
4/15/22 19:44	0.21	0.012	1.19	342.103	Ebb
4/15/22 19:52	0.78	0.014	1.19	342.103	Ebb
4/15/22 19:52	0.39	0.023	1.19	342.103	Ebb
4/15/22 19:52	-0.33	0.009	1.19	342.103	Ebb
4/15/22 19:52	0.23	0.012	1.19	342.103	Ebb

Date/Time (GMT)	Observed Runup (- tide level) (m, NAVD88)	Beta (β)	Wave Height (H_S) (m)	Wave Length (L_S) (m)	Tidal Stage
4/15/22 19:56	1.04	0.023	1.19	342.103	Ebb
4/15/22 19:56	0.58	0.016	1.19	342.103	Ebb
4/15/22 19:56	-0.26	0.006	1.19	342.103	Ebb
4/15/22 19:56	0.38	0.010	1.19	342.103	Ebb
4/15/22 19:58	1.06	0.023	1.19	342.103	Ebb
4/15/22 19:58	0.58	0.015	1.19	342.103	Ebb
4/15/22 19:58	-0.29	0.005	1.19	342.103	Ebb
4/15/22 19:58	0.38	0.009	1.19	342.103	Ebb
4/15/22 20:00	1.09	0.023	1.19	342.103	Ebb
4/15/22 20:00	0.58	0.015	1.19	342.103	Ebb
4/15/22 20:00	-0.37	0.005	1.19	342.103	Ebb
4/15/22 20:00	0.42	0.009	1.19	342.103	Ebb

LIST OF REFERENCES

Aubrey, D.G., and Speer, P.E., 1984: Updrift migration of tidal inlets. *J. of Geology*, **92,** 531–545.

Atkinson, A.L, Power, H.E., Moura, T., Hammond, T., Callaghan, D.P., and Baldock, T.E., 2017: Assessment of runup predictions by empirical models on non-truncated beaches on the south-east Australian coast. *Coast.l Eng*., **119,** 15–31.

Battjes, J.A., 1971: Run-up distributions of waves breaking on slopes. *J. Waterways Harbors Division*, **97,** 91–114.

Battjes, J.A., 1974: Surf Similarity. Proceedings of the 14th Conference of Coastal Engineering, ASCE, 466–480.

Behrens, D.K., Fabián A., Bombardelli, J.L., Largier, and Twohy, E., 2013: Episodic closure of the tidal inlet at the mouth of the Russian River — A small bar-built estuary in California. *Geomorph.*, **18,** 66–80.

Blackman, Altermatt, F., Foulquier, A., Lefébure, T., Gauthier, M., Bouchez, A., Stubbington, R., Weigand, A. M., Leese, F., and Datry, T., 2021: Unlocking our understanding of intermittent rivers and ephemeral streams with genomic tools. *Front.s Ecol. Environ.,* **19,** 574–583.

Brodie, K.L., Raubenheimer, B., Elgar, S., Slocum, R. K., and McNinch, J. E., 2015:. Lidar and Pressure Measurements of Inner-Surfzone Waves and Setup. *J. Atmos. Oceanic Technol.,* **32,** 1945–1959. https://doi.org/10.1175/JTECH-D-14-00222.

Brodie, K.L., Bruder, B. L., Slocum, R. K., and Spore, N. J. 2019: Simultaneous Mapping of Coastal Topography and Bathymetry from a Lightweight Multicamera UAS. *IEEE Trans. on Geosci. Remote Sens*., **57,** 6844–6864, doi: 10.1109/TGRS.2019.2909026.

Bruder, B. L., Hathaway, K. J., and Brodie, K. L., 2019: Design and Deployment of Mini-Argus Systems for Rapid Coastal Imaging. ERDC/CHL CHETN-IV-114. Vicksburg, MS: U.S. Army Engineer Research and Development Center. http://dx.doi.org/10.21079/11681/31463.

Carlson, C. T., 1984: Field Studies of Run-up Generated by Wind Waves on Dissipative Beaches, University Microfilms.

Commander Naval Meteorology and Oceanography Command., 2018: Commander Naval Meteorology and Oceanography Command Strategic Plan (COMNAVMETOCCOM Instruction 3120.C). CNMOC.

Coughlin, J. N., 2019: Morphology Changes to Carmel River State Beach in Relation to Waves and River Discharge. M.S. thesis, Department of Oceanography, Naval Postgraduate School, 62.

Da Silva, P.G., Coco, G. Garnier, R., and Klein, A.H., 2020: On the prediction of runup, setup and swash on beaches. *Earth-Sci. Rev.,* **204,** 103148, https://doi.org/10.1016/j.earscirev.2020.103148.

Del Toro, C., 2022: Lifelong Learning as a Strategic Imperative. 18 Aug. 2022, Naval Postgraduate School, Monterey. Keynote Address.

Department of the Navy, 2021: Unmanned campaign framework website. Accessed 03 September 2022, https://www.navy.mil/Portals/1/Strategic/20210315%20Unmanned%20Campaign_Final_LowRes.pdf.

Didier, D., Caulet, C., Bandet, M., Bernatchez, P., Dumon, D., Augereau, E., Floc'h, F., and Delacourt, C., 2020: Wave runup parameterization for sandy, gravel and platform beaches in a fetch-limited, large estuarine system. *Cont. Shelf Res*., **192,** 104024, https://doi.org/10.1016/j.csr.2019.104024.

Dodet, G., Leckler, F., Sous, D., Ardhuin, F., Filipot, J.-F., and Suanez, S., 2018. Wave runup over steep rocky cliffs. *J. Geophys. Res.: Oceans*, **123,** 7185–7205, https://doi.org/10.1029/2018JC013967.

Galvin, C.J., 1968: Breaker type classification on three laboratory beaches. *J. Geophys. Res.*, **73,** 3651–3659.

Gon, C. J., MacMahan, J. H., Thornton, E. B., and Denny, M., 2020: Wave dissipation by bottom friction on the inner shelf of a rocky shore. *J. Geophys. Res.: Oceans*, **125,** e2019JC015963. https://doi.org/10.1029/2019JC015963.

Google Earth Pro. (September 1, 2017) Pajaro River, California, USA. 36.846173°N, 121.807131W, Eye alt 2.76km [October 12, 2022].

Google Earth Pro. (November 17, 2019) Pajaro River, California, USA. 36.846173°N, 121.807131W, Eye alt 2.76km [October 12, 2022].

Guza, R.T., and Thornton, E.B., 1982: Swash oscillations on a natural beach. *J. Geophys. Res.,* **87,** 483–491.

Holland, K., Holman, R., Lippmann, T., Stanley, J., and Plant, N., 1997: Practical use of video imagery in nearshore oceanographic field studies. *IEEE J. Oceanic Eng.,* **22,** 81–92.

Holland, K.T., Lalejini, D.M., Spansel, S.D., and Holman, R.A., 2010: Littoral environmental reconnaissance using tactical imagery from unmanned aircraft systems. *Ocean Sensing and Monitoring II*. 7678, https://doi.org/10.1117/12.852952.

Holländer, L., 2022: Wave runup on rocky coasts. Thesis, Civil Engineering, Stellenbosch University, 198, https://scholar.sun.ac.za/handle/10019.1/124506.

Holman, R.A., 1986: Extreme value statistics for wave run-up on a natural beach. *Coast. Eng*., **9,** 527–544.

Holman, R.A, and Stanley, J., 2007: The history and technical capabilities of Argus. *Coast. Eng.,* **54,** 477–491.

Holman, R.A., Holland, K.T., Lalejini, D.M., and Spansel, S.D., 2011: Surf zone characterization from Unmanned Aerial Vehicle imagery. *Ocean Dyn*., **61,** 1927–1935. https://doi.org/10.1007/s10236-011-0447-y.

Holman, R.A, Brodie, K.L., Spore, N.J., 2017: Surf zone characterization using a small quadcopter: Technical Issues and Procedures. *IEEE Transactions on Geosci. Rem. Sens*., **55,** 2017–2027. https://doi.org/10.1109/TGRS.2016.2635120.

Hunt, I.A., 1959: Design of seawalls and breakwaters. *J. of Waterways Harbours Division*, ASCE 85(WW3), 123–152.

Ibaceta, R., Almar, R., Catalán, P.A., Blenkinsopp, C.E., Almeida, L.P., and Cienfuegos, R., 2018: Assessing the Performance of a Low-Cost Method for Video-Monitoring the Water Surface and Bed Level in the Swash Zone of Natural Beaches. *Rem. Sens*., **10,** 49.

Iribarren, C.R.; Nogales, C., 1949: Protection des ports. Proceedings XVIIth International Navigation Congress, Section II, Communication, vol. 4, Lisbon, 31–80.

Janušaitė, R., Karaliūnas, V., and Bevainis, L., 2019: Application of Remote Sensing Methods in Research of Nearshore Sandbars, Curonion Spit, Lithuania. *Baltic J. Mod. Comput*., **7,** 550–562, https://doi.org/10.22364/bjmc.2019.7.4.08.

Jimenez-Jimenez, S.I., Ojeda-Bustamante, W., de Jesus Marcial-Pablo, M. and Enciso, J. 2021: Digital terrain models generated with low-cost UAC photogrammetry: Methodology and Accuracy. *ISPRS International J. GeoInf*., **10,** 285, https://doi.org/10.3390/ijgi10050285.

Kastner, S.E., Horner-Devine, A.R., and Thomson, J.M., 2019: A conceptual model of a river plume in the surf zone. *J. Geophys. Res.-Oceans*., **124,** 8060–8078.

Kraus, N.C., Militello, A., and Todoroff, G., 2002: Barrier breaching processes and barrier spit breach. Stone Lagoon, California. *Shore & Beach*, **70,** 21–28.

Laudier, N.A., Thornton, E. B., & MacMahan, J., 2011: Measured and modeled wave overtopping on a natural beach. *Coast. Eng.*, **58,** 815–825. https://doi.org/10.1016/j.coastaleng.2011.04.005.

Lange, A., Fiedler, J., Merrifield, M, and Guza, R. T., 2022: UAV Video-Based Estimates of Nearshore Bathymetry. https://dx.doi.org/10.2139/ssrn.4174467.

McSweeney, S.I., Kennedy, D.M., Rutherfurd, L.D., and Stout, J.C. 2017: Intermittently Closed/Open Lakes and Lagoons: Their global distribution and boundary conditions. *Geomorph*., **292,** 142–152.

Mokrane, A., Choukchou-Braham, A., and Cherki, B., 2019: DEM Generation Based On UAV Photogrammetry. *2019 International Conference on Advanced Electrical Engineering (ICAEE)*,1–5, doi: 10.1109/ICAEE47123.2019.9014805.

Nielsen, P. and Hanslow, D.J., 1991: Wave runup distributions on natural beaches. *J. Coast. Res*., **7**, 1139–1152.

Orescanin, M.M., and Scooler, J., 2018: Observations of episodic breaching and closure at an ephemeral river. *Cont. Shelf Res*., **166,** 77–82. https://doi.org/10.1016/j.csr.2018.07.003.

Orescanin, M.M., Coughlin, and J., Young, W.R., 2021: Morphological response of variable river discharge and wave forcing at a bar-built estuary. *Estuar. Coast. Shelf Sci*., **258,** 107438, ISSN 0272–7714, https://doi.org/10.1016/j.ecss.

Pajaro River Watershed Integrated Regional Water Management (PRWIRWM) 2014: Pajaro River Watershed Integrated Regional Water Management Plan, 259, https://www.pajaroriverwatershed.org/projects/irwmp.

Palmsten M.L., and Brodie K.L., 2022: The Coastal Imaging Research Network (CIRN). *Remote Sens*., **14,** 453. https://doi.org/10.3390/rs14030453.

Ruessink, B.G., 1998: Bound and free infragravity waves in the nearshore zone under breaking and nonbreaking conditions. *J. Geophys. Res*., **103,** 12,795-12,805.

Ruggiero, P., and McDougal, W.G., 2001: An analytic model for the prediction of wave setup, longshore currents and sediment transport on beaches with seawalls. *Coast. Eng*., **43,** 161–182.

Stockdon, H.F., Holman, R. A., Howd, P. A., and Sallenger, A. H., 2006: Empirical parameterization of setup, swash, and runup. *Coast. Eng*., **53,** 573–588. https://doi.org/10.1016/j.coastaleng.2005.12.005.

Vousdoukas, M.I., Wziatek, D., and Almeida, L.P., 2012: Coastal vulnerability assessment based on video wave run-up observations at a mesotidal, steep-sloped beach. *Ocean Dyn*., **62,** 123–137.

Whitley, D., Freilich, M.H., Guza, R.T., Holmes, P., 1984: Nonlinear effects on shoaling surface gravity waves. Bifurcations of One- and Two-dimensional Maps. United Kingdom: Royal Society.

Wiegel, R.L., 1964: *Oceanographical Engineering.* Prentice Hall, Inc.

Yang, H., Li, H., Gong, Z., Dai, W., and Lu, S., 2020: Relations between the Number of GCPs and Accuracy of UAV Photogrammetry in the Foreshore of the Sandy Beach. *J. Coast. Res*., **95,** 1372–1376. https://doi.org/10.2112/SI95-263.1.

Young, W. R., 2018: Sediment Transport associated with ephemeral river breaching and closing events. M.S. thesis, Department of Oceanography, Naval Postgraduate School, 53.

THIS PAGE INTENTIONALLY LEFT BLANK

INITIAL DISTRIBUTION LIST

1. Defense Technical Information Center
   Ft. Belvoir, Virginia

2. Dudley Knox Library
   Naval Postgraduate School
   Monterey, California